A LATENT HEAT RETRIEVAL AND ITS EFFECTS ON THE INTENSITY AND STRUCTURE CHANGE OF HURRICANE GUILLERMO (1997). PART I: THE ALGORITHM AND OBSERVATIONS.

Stephen R. Guimond[1#], Mark A. Bourassa[1] and Paul D. Reasor[2]

[1]*Center for Ocean-Atmospheric Prediction Studies and Department of Earth, Ocean and Atmospheric Sciences, Florida State University, Tallahassee, FL*

[2]*Hurricane Research Division, Atlantic Oceanographic and Meteorological Laboratory Miami, FL*

Submitted to the *Journal of the Atmospheric Sciences*

October 8, 2010

[#]*Current affiliation: NASA Goddard Space Flight Center, Greenbelt, Maryland*

Corresponding author address: Stephen R. Guimond, NASA Goddard Space Flight Center, Code 613.1, Greenbelt, MD 20771.

E-mail: guimond@agnes.gsfc.nasa.gov

ABSTRACT

Despite the fact that latent heating in cloud systems drives many atmospheric circulations, including tropical cyclones, little is known of its magnitude and structure due in large part to inadequate observations. In this work, a reasonably high horizontal resolution (2 km), four-dimensional airborne Doppler radar retrieval of the latent heat of condensation/evaporation is presented for rapidly intensifying Hurricane Guillermo (1997). Several advancements in the basic retrieval algorithm are shown including: (1) analyzing the scheme within the dynamically consistent framework of a numerical model, (2) identifying algorithm sensitivities through the use of ancillary data sources and (3) developing a storage term parameterization for the precipitation budget. The determination of the saturation state is shown to be an important part of the algorithm for updrafts of ~ 5 m s^{-1} or less.

The uncertainties in the magnitude of the retrieved heating are dominated by errors in the vertical velocity. Using a combination of error propagation and Monte Carlo uncertainty techniques, biases are found to be small, and randomly distributed errors in the heating magnitude are ~16 % for updrafts greater than 5 m s^{-1} and ~156 % for updrafts of 1 m s^{-1}. Even though errors in the vertical velocity can lead to large uncertainties in the latent heating field for small updrafts/downdrafts, in an integrated sense the errors are not as drastic.

In part two, the impact of the retrievals is assessed by inserting the heating into realistic numerical simulations at 2 km horizontal resolution and comparing the generated wind structure to the Doppler radar observations of Guillermo.

1. Background and motivation

The main driver of tropical cyclone (TC) genesis and intensity change is the release of latent heat in clouds where the source of moist entropy flux comes from the thermodynamic disequilibrium at the ocean-atmosphere interface (Charney and Eliassen 1964; Kuo 1965; Emanuel 1986). In the eyewall region, convective clouds dominate the core structure with a mix of stratiform and convective features extending out to the bands of the system. Integrated cloud heating over the entire volume of the storm is believed to be responsible for intensity and structure change (Cecil and Zipser 2003; Tory et al. 2006), although full-physics modeling studies (Braun 2002) and observational composites (Black et al. 1996) show that small-scale, intense convection contributes the largest percentage of the total upward mass flux (~ 65 % from updrafts stronger than 2 m s^{-1}).

Despite the fundamental importance of latent heat release, little is known of the structure in both space and time during all phases of storm evolution. To make matters worse, balanced non-linear models of the vortex response to heating show large sensitivity to the structural characteristics (Hack and Schubert 1986). Most observational estimates of latent heat are from satellites, which have coarse resolution in both space (due to the height of the instrument as well as the limiting factors of antenna diameter and frequency choice) and time (due to orbit selection). Thus, the eyewall and rainband regions of a TC with embedded deep convective clouds are poorly resolved leading to large errors in the latent heat field.

Early satellite estimates were made using passive microwave radiometers with horizontal resolutions of ~ 25 km at nadir (Adler and Rodgers 1977). The use of passive

instruments for estimating latent heat release is difficult because of the broad, overlapping weighting functions and the complexity of the radiative transfer in clouds, especially those with mixed phase regions (Petty 2006). As a result, the specific details of hydrometeor distributions contributing to an observed brightness temperature can have large uncertainty. In addition, Adler and Rodgers (1977) and others (i.e., Sitkowski and Barnes 2009) use an estimate of the rainfall rate to compute latent heat; this approach represents a vertically integrated quantity and thus, less information on cloud structure is obtained. More recent satellite estimates use the Tropical Rainfall Measuring Mission (TRMM) Microwave Imager (TMI), which has a much higher horizontal resolution of ~ 4 - 5 km at 85 GHz. Rodgers et al. (2000) were the first to use the TMI to compute vertical profiles of latent heat in a TC and found that as the storm intensified, heating rates increased in the inner core and extended upward into the mid-upper troposphere. Recently, the TRMM Precipitation Radar (PR) has been used to estimate ~ 4.3 km horizontal and 0.25 km vertical resolution latent heating rates in TCs with three – dimensional (3D) capabilities (Tao et al. 2006).

Active instruments such as radars are not without errors either as many different drop size distributions and values of derived water content parameters, such as rainfall rate, can be associated with a measured value of reflectivity (Doviak and Zrnic 1984). As a result, latent heat estimates that rely solely on reflectivity-derived parameters can be expected to contain significant random error (a factor of nearly four for mean rainfall rate; Doviak and Zrnic 1984). As the TRMM PR is non-Doppler, critical information needed in the computation of latent heat (three components of the wind, especially vertical velocity) is unknown. In addition, the ~ 4.3 km surface footprint of the PR is still

too coarse to resolve the important details of vigorous, deep convection in TCs (Guimond et al. 2010).

Dual-polarization radar has been used to estimate warm rain and mixed phase microphysical processes in Florida convection (Tong et al. 1998). From an area-integrated perspective, Tong et al. (1998) found that warm rain processes (condensation and evaporation) dominated the total latent heat budget with a small component attributed to mixed phase processes (freezing/melting). Although very few dual-polarization observations of TCs have been published, intuition suggests that the findings of Tong et al. (1998) extend to convection in TCs.

There are not many published Doppler radar estimates of latent heat in TCs. Gamache et al. (1993) used the NOAA WP-3D (P-3) tail radars to calculate the water budget of decaying Hurricane Norbert (1984). Although no latent heat estimates were calculated, Gamache et al. (1993) showed 3D distributions of condensed water that were retrieved using the steady-state continuity equation for water. An important result from Gamache et al. (1993) was that azimuthal asymmetries accounted for nearly half the net condensation of the storm. In addition, they noted significant departures from saturation in their full 3-D retrievals whereas in the axisymmetric mean, the entire storm was saturated (except in the eye). These results, for a decaying storm, indicate that computing the latent heat field within the inner-core of TCs is not as simple as taking the product of the upward mass flux and the vertical derivative of the saturation mixing ratio. As part of the present work (including part two), the utility of determining saturation in the TC inner-core is examined in detail.

In addition to the above observational studies, several investigators have documented considerable sensitivity to numerical model microphysical schemes when simulating TC intensity and structure. McFarquhar et al. (2006) found that choice of microphysics parameterization (including alterations to the basic condensation scheme) led to variations in simulated storm intensity by nearly 10 hPa. Uncertainty in graupel characteristics were found to also produce large changes in storm intensity and are likely one of the culprits behind the consistent and significant over prediction of radar reflectivities when compared to observations (McFarquhar et al. 2006; Rogers et al. 2007).

The goal of the first part of this work is to perform a comprehensive, high-resolution, 4D, airborne Doppler radar retrieval of the latent heat of condensation in a rapidly intensifying TC. New additions to existing retrieval methods will be highlighted including detailed error characteristics. Besides providing insight into the TC intensification problem, the latent heat fields presented in this study may prove useful for the validation of space-based algorithms and provide motivation for future satellite sensors (i.e., Doppler in space).

The paper is organized as follows. In the next section, the Doppler radar platforms and data used for computing the latent heat are described. In section 3, the latent heat retrieval algorithm is presented including enhancements to existing retrieval methods. In section 4, the algorithm is applied to observations of rapidly intensifying Hurricane Guillermo (1997) and uncertainty estimates are computed. Finally, in section 5, a summary of the algorithm, conclusions and connections to part two of the work is presented.

2. Doppler radar platforms and data

The primary remote sensing instrument used in this work is airborne Doppler radar using the National Aeronautics and Space Administration (NASA) ER-2 Doppler Radar (EDOP) and the National Oceanic and Atmospheric Administration (NOAA) WP-3D (P-3) tail (TA) systems. Both platforms operate at essentially the same frequency ~ 10 GHz, yet the geometry and scanning strategies are vastly different. The EDOP has two stationary antennas, one pointed at nadir and the other 33° off-nadir. Measurements from EDOP are taken from the high-altitude (20 km) ER-2 aircraft (able to overfly intense convection) every 0.5 s with a 200 m s^{-1} ground speed providing some of the finest sampling of any current airborne radar (100 m along-track with a typical 37.5 m gate spacing; Heymsfield et al. 1996). The along-track spacing results in significant oversampling of precipitation yielding an effective horizontal resolution between 100 m and the 2.9° beamwidth (i.e., ~ 0.55 km at surface and ~ 0.30 km at 10 km altitude). The main advantage of EDOP is the nadir-viewing geometry that provides direct measurements of the vertical component of Doppler velocities relative to the aircraft and superior resolution when compared to scanning radars. A major disadvantage of EDOP is the inability to retrieve the three components of the wind and 3D features, as the non-scanning beams only measure Doppler velocities along the vertical plane of the aircraft track. In addition, for track headings not aligned along a Cardinal direction, the along-track wind structure is often complicated and difficult to interpret.

The P-3 TA radar scans 360º in a plane perpendicular to the flight track and often employs the fore/aft scanning technique (FAST) in which the antenna scans in a cone

offset from the track-normal plane alternately fore and aft of the aircraft. The aircraft typically flies between 3 – 4 km altitude and does not penetrate convective cores, relying on side-looking views of high reflectivity regions. The along-track sampling of the P-3 TA radar in normal-plane scanning mode and FAST mode is ~ 0.75 km and ~ 1.5 km, respectively with 0.15 km gate spacing (Gamache et al. 1995; Black et al. 1996). Taking into account the 1.9° vertical and 1.35° horizontal beamwidths of the TA antennae and the sampling intervals using FAST, grid resolutions from the P-3s range from 1.5 – 2.0 km in the horizontal to 0.5 – 1.0 km in the vertical (Reasor et al. 2000; Reasor et al. 2009). The main advantage of the P-3 radar sampling is the ability to provide essential information on the three wind components through the use of a retrieval technique (Gamache 1997; Gao et al. 1999; Reasor et al. 2009). In addition, the P-3 database is much more extensive than that from EDOP. However, the relatively coarse resolution of the analyses, the need to solve for the vertical velocity and contamination of much of the boundary layer from ocean surface backscatter are the primary drawbacks of the P-3 TA radar relative to EDOP.

The EDOP data utilized in this study is compiled from multiple NASA field experiments yielding thirteen vertical profiles of deep convective updrafts in TCs (Heymsfield et al. 2010). The peak vertical velocity of the mean profile was ~13 – 14 m s^{-1} while individual members had values as high as 25 m s^{-1} located at 12 – 14 km in height. Guimond et al. (2010) describes the detailed structure of two "hot tower" samples from the Heymsfield et al. (2010) population occurring within the eyewall of rapidly intensifying Hurricane Dennis (2005). In the present study, a hot tower is defined as a special class of deep convection: updraft profiles from the Heymsfield et al. (2010) TC

sample with maximum vertical velocity values in the top 38 % of the population (results in five profiles, which are shown in Fig. 1 along with the mean). See Heymsfield et al. (2010) for more information on these data. The mean of this hot tower sample is considered to represent mature updrafts near peak intensity. Note that this dataset likely represents the highest quality (resolution, direct measurement of vertical Doppler velocity) updraft structure currently available in TCs and deep convection. Further studies of EDOP data in TCs including comparisons to in situ data can be found in Heymsfield et al. (2001).

The P-3 data analyzed here were collected by two aircraft in the core of Eastern Pacific Hurricane Guillermo on 2 August 1997 for ~ 5.5 hours (10 composite periods with ~ 34 minute sampling frequency) coincident with a rapid intensification episode of the storm (Reasor et al. 2009). Weak to moderate vertical wind shear (7 – 8 m s^{-1}) resulted in a preference for convection in the downshear left quadrant of the storm during this period. Low wavenumber vorticity asymmetries propagating around the vortex were found to excite strong convective bursts that coincided with the greatest intensification (Reasor et al. 2009). Figure 2 shows reflectivity scans from the NOAA P-3 lower fuselage radar (5.3 GHz) at 3 km altitude during ten eyewall penetrations on 2 August 1997. Oscillations in the structure of the reflectivity from asymmetric to more axisymmetric can be seen in Fig. 2 along with evidence of the presence of several convective bursts.

Given the consecutive sampling and spatial coverage, the Guillermo dataset provides the opportunity for studying fundamental problems associated with the impacts of deep convection and the role of the asymmetric mode in TC intensification. However, coarse

resolution of the Doppler analyses in space and time still limits the interpretation of the basic physics. The storm-centered radar domain is a box extending 120 km on a side with 2 km grid spacing and 20 km in the vertical with 1 km grid spacing. The first level of useful data is at 1 km height due to ocean surface contamination. Guillermo's 3-D wind field was retrieved using a variational approach on a system of equations that includes the radar projection equations, the anelastic mass continuity equation and a Laplacian filter, among others, including boundary conditions for the surface and just above the echo top (Gamache 1997; Gao et al. 1999; Reasor et al. 2009). Regions of the domain that do not have Doppler velocity information (such as portions of the eye) are effectively interpolated/extrapolated from regions where Doppler velocity was observed through a Laplacian filter (Reasor et al. 2009). The radar scanning strategies employed in the Guillermo sampling requires a finite time separation between radial wind measurements in order to construct an accurate wind vector. Reasor et al. (2009) found a maximum time separation of ~ 6 min on the edges of the Guillermo Doppler domain and much less in the eyewall region (~ 3 min) indicating relatively small impact on the present analysis, which focuses on the eyewall. This radar dataset is used to perform a latent heat retrieval, described in detail in the next section.

3. Latent heat retrieval algorithm

The technique for retrieving latent heat from airborne Doppler radar is based partly on the method of Roux (1985) and Roux and Ju (1990). These studies used simplified forms of the momentum and thermal energy equations, with individual terms or forcings estimated from radar observations, to deduce the pressure and temperature fields of squall

lines. We focus our attention on the computation of saturation (see appendix B of Roux and Ju 1990) and the use of the thermal energy equation. Several advancements in the basic algorithm are developed and presented below including: (a) analyzing the scheme within the dynamically consistent framework of a numerical model, (b) identifying sensitivities through the use of ancillary data sources and (c) developing a precipitation budget storage term parameterization.

a. Theory

To prove the efficacy of the retrieval method, output from a non-hydrostatic, full-physics, quasi cloud-resolving model simulation of Hurricane Bonnie (1998) at 2-km horizontal grid spacing (Braun et al. 2006; Braun 2006) is examined. The focus here will be on a one hour period of the simulation (domain size of ~ 450 km^2 in the horizontal extending to 17.2 km in the vertical with the first model level at 40 m above the ocean) where model variables and precipitation budget terms were output every three minutes. At this time, the simulated storm was intensifying despite the influence of northwesterly vertical wind shear that resulted in an asymmetric distribution of convection (see Braun et al. 2006 and Braun 2006 for a detailed description of Hurricane Bonnie and the numerical simulation). Although the simulated TC does not replicate the observed storm, the dynamically consistent nature of the model budgets allows the assessment of the qualitative and, to some degree, quantitative accuracy of the method. Gao et al. (1999) used numerical model output to test the accuracy of a Doppler radar wind retrieval algorithm and found errors (see their table 1) that are consistent with those computed from *in situ* data using a similar retrieval algorithm (e.g. see table 2 of Reasor et al.

2009). More real cases are needed to determine if the quantitative aspects of the Gao et al. (1999) results are valid, but the qualitative accuracy appears robust.

The release of the latent heat of condensation occurs when water vapor changes phase to liquid water, which requires the air to be saturated. Therefore, for strong updrafts, analysis of the vertical momentum equation reveals that local buoyancy from the release of latent heat must be present to generate significant vertical wind speeds and accelerations (Braun 2002; Eastin et al. 2005). Therefore, an important question is: does a threshold of vertical velocity exist where saturation and the release of latent heat can be assumed? Figure 3 (courtesy of Dr. Matt Eastin) shows 620 updraft cores (defined as convective-scale vertical velocities that exceed 1.0 m s^{-1} for at least 0.5 km along the flight track) as a function of relative humidity from P-3 flight level (1.5 – 5.5 km altitude) measurements in the eyewall and rainband regions of 14 intense TCs (Eastin et al. 2005). At 5.0 m s^{-1} and below, large variability in relative humidity is observed while above 5.0 m s^{-1}, nearly all updraft cores are saturated. Levels above ~ 5.5 km are not sampled by the aircraft. This data suggests that using a vertical velocity saturation threshold of ~ 5.0 m s^{-1} is reasonable although the sample size is small.

The numerical simulation of Hurricane Bonnie is used to calculate basic statistics on saturated vertical velocities (on a grid point by grid point basis for which there are 226×226×27 points in the domain) to compare to the observational data. Over the one hour portion of the simulation analyzed here, approximately 52% of grid points with an updraft are unsaturated with 94% of these coming from values less than 1 m s^{-1}. More importantly, ~ 92% of grid points with updrafts greater than 5 m s^{-1} are saturated (95,635 out of 104,074 points) which corroborates the observational data shown in Fig. 3. A

similar result is found for downdrafts. Based on this data, we conclude that a threshold of $|w| > 5$ m s^{-1} is reasonable for assuming saturation. Above 5 m s^{-1}, vertical accelerations are dominated by local buoyancy forcing while below 5 m s^{-1} various physical processes may play a role in the evolution such as perturbation pressure gradient forces (that are not generated by heating) and turbulence (Braun 2002; Eastin 2005). This threshold should only be used as a guide as updrafts likely do not obey strict rules, but rather evolve through a continuum. Statistics computed from the Bonnie simulation revealed that ~ 99% of updrafts are found to be less than or equal to 5 m s^{-1}, which carries the vast majority of the upward mass flux (~ 70 %; Black et al. 1996; Braun 2002). As a result, saturation cannot be assumed for the vast majority of updrafts and a large percentage of the total mass flux, which motivates the need for the determination of saturation through the algorithm described below.

The simplified form of the full model equation for the continuity of total precipitation mass (rain, snow and graupel) can be written in a manner similar to Braun (2006),

$$\frac{\partial \rho q_p}{\partial t} = -\nabla \bullet \left(\rho q_p \vec{u}\right) - \frac{\partial \left(\rho q_p w\right)}{\partial z} + \frac{\partial \left(\rho q_p V_t\right)}{\partial z} + \rho Q_+ - \rho Q_- + \rho D + \rho Z \,, \qquad (1)$$

where ρ is the dry air density, q_p is the total precipitation mixing ratio in kg kg^{-1}, V_t is the hydrometeor fallspeed in m s^{-1}, Q_+ and Q_- are the total precipitation sources and sinks (units of kg kg^{-1} s^{-1}), respectively, D is the diffusive tendency of q_p and Z is an artificial model offset for negative mixing ratios. The horizontal winds ($\vec{u}$) are storm-relative and w is the vertical velocity all in m s^{-1}. Examination of each budget term (see Braun 2006 for a description of some terms) on the convective scale (20 by 15 km horizontal mean centered on strong eyewall convection and single grid points within an

eyewall convective cell) revealed that the turbulent diffusion of precipitation and model offset terms are small and can be neglected. These results are consistent with Braun (2006). The reduced form of the continuity equation for total precipitation mass used in this study becomes

$$\frac{\partial \rho q_p}{\partial t} \cong -\nabla \bullet \left(\rho q_p \bar{u}\right) - \frac{\partial \left(\rho q_p w\right)}{\partial z} + \frac{\partial \left(\rho q_p V_t\right)}{\partial z} + \rho Q_{net}, \tag{2}$$

where the sources and sinks of precipitation mass are combined into a net precipitation source term (Q_{net}). We note that the second and third terms on the right-hand-side of (2) can be combined to yield a vertical Doppler velocity flux divergence of precipitation, which reduces errors in the budget (avoids estimation of hydrometeor fallspeeds). However, combining these terms can only be done when the radar antenna is positioned in vertical incidence, which was not the case for the P-3 sampling of Guillermo (FAST was employed).

Figure 4 shows a scatter plot of the relationship between Q_{net} (output from model) and the source of cloud water (condensation, indicating saturation) at model grid points where precipitation is produced between 0 – 10 km height in the first nine minutes (with three minute output) of the one hour simulation period. This subset of data is representative of the entire simulation and includes 828,611 points. A height of 10 km is used as a cap for points in Fig. 4 because the simulation revealed that the source of cloud water ceased at this level in deep convection (see Fig. 5 for an example). The points in Fig. 4 are colored by temperature with red points > 0°C (rain microphysics) and blue points ≤ 0°C (ice microphysics). There is a linear relationship between the two variables in Fig. 4 with ~70 % of the variability (statistic computed for the entire one hour period)

in Q_{net} explained by the source of cloud water for all points (rain and ice processes). The dominant mode of precipitation growth shown in Fig. 4 is rain microphysics and the associated collision-coalescence process (Rogers and Yau 1989) with the source of cloud water explaining 87% of the variance in Q_{net} for rain microphysics (red points) only.

Braun (2006) showed that in the azimuthal mean, the source of cloud water in the eyewall is immediately removed by precipitating hydrometeors (collision-coalescence process), which is shown here on the grid point scale. The off-linear scatter in Fig. 4 is explained by ice microphysics (blue points) taking over the net production of precipitation. Note that there is some overlap between the red and blue points (mostly near the freezing level) because no discrete threshold for rain/ice microphysics exists. Indeed, observations suggest that super cooled cloud liquid water can exist at altitudes of 12 km in deep convection located in the TC eyewall (Black et al. 2003).

Figure 5 shows an example of the vertical structure of the relationship between Q_{net} and the source of cloud water for convection in the Bonnie simulation (averaged over a representative eyewall convective cell). The source of cloud water matches very well with the net production of precipitation up to 5 – 6 km height (melting zone). Above 6 km height, ice phase microphysics begins contributing to the formation of precipitation. A similar vertical structure is found for other regions (eyewall and rainbands) of the simulation domain.

In summary, Figs. 4 and 5 demonstrate that by acquiring information on Q_{net} and determining where $Q_{net} > 0$ (net production of precipitation), we are able to distinguish where the air is saturated, which is required before the release of latent heat can take place. Knowledge of the possible microphysical sources of precipitation (Rogers and

Yau 1989) suggests that this is also true of TCs in nature. Note that equation (2) and the association of $Q_{net} > 0$ with saturation are valid *instantaneously*. That is, assuming information on the water content and winds are available quasi-instantaneously, the saturation state of the air and the associated magnitude of the latent heat release (described below) can be determined at the same time. Therefore, by using the signal radar responds to (precipitating hydrometeors for 10 GHz) information on the saturation state (and latent heat release) at each grid point in the 3-D Doppler domain can be retrieved.

There are errors in associating the net production of precipitation with saturation in mixed phase regions of convection and for small values of Q_{net} which could occur near cloud boundaries, for example. When applying the theory to radar observations, instrument errors are also possible due to resolution, non-homogeneous beam filling, attenuation and calibration. Another source of error is the time separation between radar beam intersections discussed in section 2 that violates the instantaneous assumption. However, the algorithm presented here is somewhat insensitive to these errors because information is only required on the *condition* of saturation, not the *magnitude* of that saturation. Relying on Q_{net} for quantitative purposes (such as computing the latent heat magnitude) can lead to significant errors due to the large uncertainty in single frequency radar derived water parameters (see introduction; Gamache et al. 1993). We focus on the qualitative nature of Q_{net} to reduce the consequences of these errors, although dual-frequency radars show promise for quantitative retrievals of Q_{net} in future studies. With the P-3 radar used in this study, substantially reduced errors in the latent heat magnitude

can be achieved by using the radar estimates of vertical velocity directly (described below) rather than relying on Q_{net} quantitatively.

Once the saturation state is determined, the magnitude of the latent heat can be calculated according to the entropy form of the first law of thermodynamics,

$$C_p \frac{D \ln \theta}{Dt} = \frac{J}{T} \tag{3}$$

where C_p is the specific heat of dry air at constant pressure (1004 J K^{-1} kg^{-1}), θ is potential temperature in K, T is temperature in K and D/Dt is the material derivative. The heating rate term in (3) takes the form $J = -L_c \frac{Dq_s}{Dt}$ with L_c the latent heat of condensation at 0 °C (2.50×10^6 J kg^{-1}) and q_s is the saturation mixing ratio in kg kg^{-1}. The material rate of change of the saturation mixing ratio, which is a function of temperature and pressure, is dominated by the vertical advection yielding an approximate expression for the heating rate term, $J \cong -L_c w \frac{\partial q_s}{\partial z}$. Note that other diabatic contributions to the thermal energy budget such as radiative effects have been neglected. Substituting the approximate heating rate term into (3) and rearranging yields the expression used to calculate the magnitude of the latent heat release

$$\frac{D\theta}{Dt} \cong \frac{-L_c \theta}{C_p T} w \frac{\partial q_s}{\partial z}. \tag{4}$$

This method provides information on the latent heat of condensation/evaporation only and does not include mixed phase processes. However, as mentioned in the introduction, the overwhelming contribution to the total latent heat and thermal energy budget in convection comes from warm rain processes (Tong et al. 1998; Zhang et al. 2002).

Figure 6 presents a flowchart summarizing the main steps in the latent heat retrieval algorithm described above. The two main steps are: (a) solve equation (2) for the net production of precipitation (Q_{net}) and identify regions of saturation ($Q_{net} > 0$) and (b) in regions of saturation, compute the magnitude of latent heating or evaporative cooling using equation (4).

b. Examining the assumptions in computing saturation

Previous studies employing a form of the retrieval method outlined above have been unable to calculate the storage (local tendency) term in (2) due to inadequate Doppler radar sampling and, thus, assumed the system or the clouds were in a steady state (Roux 1985; Roux and Ju 1990; Gamache et al. 1993). In a storm-relative reference frame, both the cloud and system scales of motion are not steady state and significant error can be expected if assuming stationarity (Gamache 1993), especially on a local scale. The Guillermo dataset is unique in that composite Doppler radar sampling was completed on average every 34 minutes allowing estimation of the storage term. However, it is found that using a 34 minute time increment for computing the storage term added no more information (order of magnitude smaller than other terms) to the precipitation budget than using the steady state assumption. This result is not surprising considering the lifecycle of a cloud is on the order of 30 minutes (Houze 1993).

How important is the storage term in the current latent heat retrieval algorithm for more accurate (shorter time update) values? To address this question, a parameterization of the storage term is derived using output from the Bonnie numerical simulation. For model grid points where precipitation is produced, a linear relationship between the total horizontal advective flux of precipitation (largest contribution from tangential

component) and the storage of precipitation (output directly from model with a time step of a few seconds) is found (see Fig. 7). Note that Fig. 7 only includes data at one snapshot while the linear fit used to derive the regression relation ($R^2 = 0.78$),

$$\frac{\partial \rho q_p}{\partial t} = 0.802 \times \left[-\nabla \bullet \left(\rho q_p \bar{u} \right) \right] \quad (5)^1$$

utilized an average of the fits at three minute intervals over a one hour period. The strong relationship in (5) does not imply that the saturation signal (Q_{net}) is a small residual and therefore prone to large error. The magnitude of Q_{net} is analyzed on several scales (grid point, spatial and temporal averages in convective/stratiform regions) and is found to have a significant signal relative to the other terms in equation (2). Physically, the relationship in (5) confirms the fact that the tangential advective transport of precipitation in a mature TC controls the storage of precipitation to a large degree (a consequence of the divergence theorem). This relationship indicates that morphing (Wimmers and Velden 2007) the radar reflectivity and derived precipitation fields using the Doppler wind analyses to generate a storage term tendency shows promise. The storage term values produced through the model-based parameterization are very similar to those calculated from ground-based radar (refresh time of ~5 minutes) and P-3 LF radar (refresh time of 30 s) observations of mature TCs (not shown).

For the Bonnie simulation, Fig. 8 shows that using the storage term parameterization in (5) reduces the root mean square error (RMSE) in Q_{net} by more than a factor of two relative to the steady state case. This result can also be expressed in terms of a cylindrical volume integrated error,

$$Error = \frac{\left| \int_0^z \int_0^r \overline{X^P} r dr dz - \int_0^z \int_0^r \overline{X^O} r dr dz \right|}{\int_0^z \int_0^r \overline{X^O} r dr dz} \tag{6}$$

where $\overline{X^P}$ is the azimuthal mean of the predicted variable (in this case, the estimate of Q_{net} under various approximations), $\overline{X^O}$ is the azimuthal mean of the observed variable (in this case, Q_{net} output directly from the model) and *r* and *z* are the chosen outer (200 km) and upper (17 km) boundaries of the domain, respectively. Figure 9 depicts a time series of (6) for Q_{net} revealing that in the temporal mean, the storage term parameterization reduces the error in Q_{net} by ~ 16 % with improvements of nearly 30 % at various times using the numerical model output. Also shown in Figs. 8 and 9 is the error using the approximate form of the precipitation continuity equation in (2) with Q_{net} output directly from the model serving as the control. The errors in using (2) are low, which is consistent with the scale analysis already discussed.

We have demonstrated that Q_{net} is a very good proxy for saturation in a numerical setting. In addition, a reduced form of the precipitation continuity equation with a parameterization of the storage term has been shown to provide a good diagnosis of the actual Q_{net} output from the model. An obvious question is: what is the impact of these approximations on the derived latent heating?

Figure 10 shows the impact of the storage term parameterization in terms of the azimuthal mean latent heating at the radius of maximum wind (RMW) for the Guillermo Doppler radar observations (shown in the next section). This sensitivity analysis is shown here because our ultimate goal is to apply the algorithm to observations. Large

changes to the azimuthal mean heating relative to the steady state case are found when using the parameterization (see Fig. 10) with differences of ~ 20 % at mid-levels to over 100 % at lower (3 km) and upper (10 km) levels. Recent research has shown that for simplified TC-like vortices, the azimuthal mean heating dominates the dynamics of TC intensification (Nolan and Grasso 2003; Nolan et al. 2007). In light of these results, the storage term sensitivity shown in Fig. 10 is not only quantitatively significant for the accurate retrieval of latent heating in TCs such as Guillermo; it is physically significant as well.

Figure 11 shows the errors (according to equation 6) in computing latent heat by determining saturation using equations (2) and (5) and identifying where the values of Q_{net} are greater than zero. The control is computing latent heat at grid points that are producing cloud water, which is required for air to be saturated. Note that latent heating rates computed from the model's microphysical scheme were not available, so the diagnostic latent heating rate (considering updrafts only) in (4) is used instead. Differences between the latent heating rates should be small and the expression in (4) is currently the only practical way to compute them from radar observations. The temporal mean error in Fig. 11 is ~ 8% with ~ 93% of the variance in the azimuthal mean heating explained by the retrieval method. Errors computed using both updrafts and downdrafts showed similar results albeit with a weaker explained variance (~ 87%).

The results described above demonstrate that the method for determining saturation in the latent heat retrieval is quite reasonable. Validating this result using observations is difficult because of the lack of in situ data over the large swaths sampled by the radar. Using a combination of flight level data and dropsondes offers the best avenue for

validation and is left for future work. Sensitivity tests and observational error analyses of the diagnostic heating expression in (4) are detailed in the next section.

4. Observations and errors

a. Doppler radar derived latent heating

To compute saturation (Q_{net}) from Doppler radar, the total precipitation mixing ratio must be known. In order to derive this quantity, in situ cloud particle data collected by NOAA P-3 aircraft at ~ 4 km altitude in the intense stages of Hurricane Katrina (2005) is analyzed. The cloud particle data is averaged over a period of 6 s in an attempt to match the sampling volumes of the particle probe and Doppler radar pulses (Robert Black, personal communication). Using the cloud particle data, radar reflectivity factor (Z) and liquid water content (LWC) are computed and the coefficients (A and B) of the power law ($Z = A \times LWC^B$) are determined. Figure 12 shows a scatter plot (~ 7,000 data points) of the relationship between reflectivity factor (expressed in dBZ) and LWC for the Katrina data. The red line shows the best fit ($Z = 402 \times LWC^{1.47}$) with a correlation coefficient of 0.88 while the blue lines depict the 95% confidence interval, which gets larger with higher reflectivities (partly due to sampling). The relationship $Z = 402 \times LWC^{1.47}$ is used below the melting layer while the ice water content (IWC) parameterization $Z = 670 \times IWC^{1.79}$ (Black 1990) is used above the melting layer with linear interpolation of the two expressions within the melting layer.

Note that relationships between radar reflectivity factor and water content parameters are not unique and therefore, uncertainty in Q_{net} will exist. As mentioned in the previous section, however, the algorithm presented here is *somewhat* insensitive to these errors

because information is only required on the condition of saturation, not the magnitude of saturation. Equation (2) is solved for Q_{net} using the Guillermo Doppler analyses, the storage term parameterization in (5), the computed precipitation mixing ratios described above and hydrometeor fall speed relations for a gamma distribution (Ulbrich and Chilson 1994; Heymsfield et al. 1999). Based on Fig. 3 and the discussion in the previous section, grid points with $|w| > 5$ m s^{-1} are assumed saturated.

To compute the magnitude of latent heat released at saturated grid points in the radar domain, knowledge of the thermodynamic structure of convective cells is required, which is very difficult to obtain. To approximate the thermodynamic structure, a composite high-altitude (using NASA aircraft that fly at altitudes of 10 and 20 km) dropsonde representative of eyewall convection in TCs is utilized. The storms sampled were: Hurricane Bonnie (1998), Tropical Storm Chantal (2001), Hurricane Gabrielle (2001), Hurricane Erin (2001) and Hurricane Humberto (2001) yielding ten independent thermodynamic profiles of eyewall convection. The sampling of eyewall convection is verified using winds and relative humidity from the dropsondes as well as satellite observations. Discussion on the uncertainty associated with using a composite dropsonde is discussed below. To complete the latent heat calculation, the vertical velocities derived from the Doppler radar synthesis procedure are input to equation (4). The latent heat of condensation is capped at 10 km altitude based on independent numerical simulation experiments and the structure of the cloud water source shown in Fig. 5.

Figure 13 displays 3D snapshots of the derived latent heat field (+/- 100 K h^{-1} isosurface) in Hurricane Guillermo (1997) for each aircraft pass in Fig. 2. The structure in Fig. 13 is consistent with the 3-km altitude reflectivity scans shown in Fig. 2. Initially

(Fig. 13, pass 1), the latent heat field is quite asymmetric with convection displaced to the down-shear quadrants of the storm due to the persistent vertical shear forcing of the vortex (Reasor et al. 2009). This low-wavenumber latent heat asymmetry is coupled to the vorticity field (Reasor et al. 2009) as the features propagate around the eyewall of Guillermo occasionally revealing a more symmetric distribution of convection (Figs. 2 and 13, passes 2 – 5 and 7). Passes 6, 7 and 9 in Fig. 13 show the emergence of large, individual pulses of heating (and cooling) with peak magnitudes between 200 – 300 K h^{-1}. Reasor et al. (2009) found that these strong convective bursts coincided with the largest intensification of Guillermo and were triggered by convergence associated with low-wavenumber vorticity asymmetries in the eyewall. The full observational period (~ 5.5 h) of the latent heat retrievals presented in Fig. 13 are used as time-dependent forcing in a non-linear numerical model in order to examine their impacts on numerically simulated intensity and structure change. This is the topic of part two.

Figure 14 shows the latent heat profile computed using the mean EDOP vertical velocity data presented in Fig. 1 and the composite thermodynamic data discussed above. Almost the entire mean profile in Fig. 1 is greater than 5 m s^{-1} and therefore, saturation is assumed. The mean EDOP latent heat profile is shown because of the high quality of the data (very high resolution and direct measurement of vertical Doppler velocities relative to the aircraft), which may be a useful reference for the community. The authors are currently using the profile in Fig. 14 to understand the dynamic response of a realistic TC vortex to observational heating perturbations.

b. Uncertainty estimates

There are two main calculations in the retrieval that require error analysis: the computation of the saturation state and the magnitude of the latent heat. The approximate errors associated with determining saturation are analyzed in section 3b and thus, the focus here is on the magnitude of the latent heat fields. The magnitude of the latent heat is essentially a function of thermodynamic information (temperature and pressure) and vertical velocity. The uncertainty in the thermodynamic information is assessed by first gathering soundings from various regions (eyewall and environment) of the numerical simulation of Hurricane Bonnie and eyewall dropsonde observations in several storms (see section 4a for the list of TCs). These thermodynamic profiles are then input to equation (4) revealing differences in the peak latent heat of only ~ 10 – 15 %. These results indicate that the magnitude of the latent heat is not very sensitive to the details of the thermodynamic information in the eyewall of TCs.

Sensitivity to the vertical velocity is much greater and is the most important parameter in the estimation of latent heat. Reasor et al. (2009) compared the Guillermo Doppler radar analyzed vertical velocities to flight-level *in situ* measurements and found a RMSE of 1.56 m s^{-1} in the eyewall region with a correlation coefficient of 0.61. Morrow (2008) compared a large set of P-3 derived wind fields with flight-level wind measurements, including those from Guillermo, and found that overall the intense and wide updrafts were captured well by the Doppler analysis while those that were narrow and weaker were not well represented. This result extends to downdrafts as well (Morrow 2008; Reasor et al. 2009)

Figure 15 (from Morrow 2008) shows a representative comparison of flight-level vertical velocities (at ~3 km altitude) to those computed from the Doppler analysis valid

at ~ 2002 UTC 2 August 1997 in Hurricane Guillermo. The strong, wide updraft pulse at 30 km radius is represented well by the Doppler analysis as are the general patterns of the vertical velocity field, but the narrow updrafts/downdrafts are clearly not captured. These errors are likely a result of: (1) inadequate matching of the radar and flight-level sampling volumes and resolutions and (2) the need to use the anelastic mass continuity equation (more specifically, divergence) to solve for the vertical velocity. For the 2 km horizontal resolution of the Guillermo dataset (which relies heavily on FAST), the vertical velocity is estimated by computing divergence from data over an area of 16 km^2, which effectively filters out smaller scale perturbations (Marks et al. 1992). In addition, surface contamination does not allow adequate computation of divergence in the boundary layer, which will lead to errors in the vertical velocity aloft.

The random error in the latent heat magnitudes can be estimated through an error propagation analysis. The general formula for error propagation is

$$\delta q^2 = \sum_i \left(\frac{\partial q}{\partial x_i} \delta x_i \right)^2, \tag{7}$$

where δq represents the Gaussian uncertainty in q (a function of x_i), and each x_i denotes a variable with associated uncertainty δx_i that contributes to the calculation of δq.

Applying (7) to equation (4) yields

$$\delta^2_{D\theta/Dt} = \left(\frac{-L_c}{C_p} \right)^2 \left[\left(\frac{w}{T} \frac{\partial q_s}{\partial z} \delta_\theta \right)^2 + \left(\frac{\theta}{T} \frac{\partial q_s}{\partial z} \delta_w \right)^2 + \left(\frac{-\theta}{T^2} w \frac{\partial q_s}{\partial z} \delta_T \right)^2 + \left(\frac{\theta}{T} w \delta_{\partial q_s / dz} \right)^2 \right]. \tag{8}$$

The uncertainties in each variable in (8) are determined from standard deviations in the dropsonde data described in section 4a and the RMSEs in vertical velocity from the Reasor et al. (2009) study: $\delta_T = 2.5\,\mathrm{K}$, $\delta_\theta = 3.1\,\mathrm{K}$, $\delta_{\partial q_s/\partial z} = 3.4 \times 10^{-7}\ \mathrm{m^{-1}}$ and

$\delta_w = 1.56$ m s^{-1}. For all other variables in (8), characteristic values for the TC eyewall are chosen: $T = 300\,\mathrm{K}$, $\theta = 302\,\mathrm{K}$, $\frac{\partial q_s}{\partial z} = -4\times10^{-6}$ m^{-1} and $w = 5$ m s^{-1}. The second term on the right-hand-side of (8) is larger than the other terms by at least an order of magnitude. Using this information and expressing the uncertainty in the latent heat magnitude as a percentage ($U_{D\theta/Dt}$) yields the following simplified equation

$$U_{D\theta/Dt} \cong \left|\frac{\delta w}{w}\right| \times 100\,. \tag{9}$$

Plugging in the characteristic values chosen above and assuming the RMSEs computed in Reasor et al. (2009) are representative of a spectrum of vertical velocities, the uncertainty in the latent heat magnitude for updrafts of 5 m s^{-1} is ~ 32 %. For smaller vertical velocities the errors can be large: a 1 m s^{-1} updraft has an uncertainty in latent heat magnitude of ~ 156 %. The errors in the latent heat magnitude are dominated by random errors, although a slight positive bias of 0.16 m s^{-1} in the eyewall vertical velocities was found by Reasor et al. (2009), indicating that the latent heat retrievals may produce too much heat on average. However, when combining the biases in the latent heat magnitude and structure (through the calculation of saturation), the sign of the total bias in the retrievals is not clear although it is small compared to the random errors. Part two of this study will attempt to address the combined error issue by analyzing the ability of the latent heat fields to reproduce the observed wind speeds of Guillermo using a numerical model.

The discussion above estimates the uncertainties with computing the latent heat magnitude. Another source of uncertainty is discovered by asking the question: how well does the Guillermo dataset represent a larger distribution of convection and latent

heat in TCs? This type of error is referred to as a sampling uncertainty. The updrafts (and latent heat) in Guillermo were log-normally distributed as are most TCs (Black et al. 1996) and require more advanced statistics than those of Gaussian distributions to describe their sampling uncertainties. We are interested in the sampling errors associated with deep convection and therefore, a subset of the latent heat field is selected for statistical analysis (vertical velocities greater than 5 m s^{-1}) shown in the histogram in Fig. 16.

In order to estimate the sampling uncertainty in the mean value of this subset (117 K h^{-1}), a Monte Carlo based method called the "bootstrap" is utilized. Estimation of the uncertainty in the mean (including the bootstrap method) is sensitive to the degrees of freedom in the dataset. To estimate the degrees of freedom in the latent heat field over the full 3-D domain and for all ten composite periods, a combination of statistical (auto-lag correlation) and physical reasoning is employed. An auto-lag analysis in time reveals that each grid point in the Doppler domain has a time scale for independence of about 30 minutes (convective lifetime), while one degree of freedom in the vertical is assumed to represent a column of the atmosphere. An auto-lag analysis in the horizontal directions through deep convective cells reveals an independent spatial scale of ~ 12 km in each direction (approximate deep convective cell size in P-3 data). The number of degrees of freedom (DOF) is then calculated as

$$DOF = \frac{T_x T_y T_z T_t}{I_x I_y I_z I_t} \alpha \,, \tag{10}$$

where T_i are the number of grid points in a dimension, I_i are the length and time scales for independence in each dimension, and α is the percentage of the total sample being considered (3% for vertical velocities greater than 5 m s^{-1}). Using the scales discussed

above along with (10), 30 degrees of freedom (or independent deep convective cells) are found in the Guillermo radar dataset.

The bootstrap is performed through the following two steps. First, a random number generator with a discrete uniform distribution is used to create 1000 perturbed latent heat datasets each with a sample size of 30 (degrees of freedom) from the observed distribution shown in Fig. 16. Second, averages are computed for each dataset and they are sorted in ascending order. Using the sorted data, the 25^{th} and 975^{th} values are selected yielding the 95% confidence interval for the mean latent heat rate in the observed distribution (117 K h^{-1}; Fig. 16) of 101 – 133 K h^{-1} (or 14 %). This sampling uncertainty is lower than the standard uncertainty found for updrafts of 5 m s^{-1} (~ 32 %) because of the distribution of data considered in the sampling case (updrafts > 5 m s^{-1}). Plugging the maximum updraft analyzed in the Guillermo P-3 dataset (~ 30 m s^{-1}) into (9) along with the approximate uncertainty of 1.56 m s^{-1} yields an error of ~ 5 %. Averaging this 5 % error value with that for a 5 m s^{-1} updraft (32 %) yields a mean error of 18.5 %; this is close to the sampling uncertainty.

5. Summary and conclusions

In this paper, a revised algorithm for computing the latent heat associated with warm rain microphysics (condensation and evaporation) in TCs from airborne Doppler radar observations is presented. Several advancements in the basic algorithm (Roux 1985; Roux and Ju 1990) are developed including: (a) analyzing the scheme within the dynamically consistent framework of a numerical model, (b) developing a precipitation

budget storage term parameterization and (c) identifying sensitivities and errors in the retrievals through the use of ancillary data sources and uncertainty analysis.

The determination of the saturation state is shown to be an important part of the algorithm. While strong vertical velocities will virtually always be saturated in order to provide the necessary buoyancy forcing (Braun 2002; Eastin et al. 2005), weak to moderate vertical velocities require calculation or observation of the saturation state. Analysis of flight-level data in the inner-core of intense hurricanes as well as a high-resolution numerical model simulation of Hurricane Bonnie (1998; Braun 2006) advocates that for $|w| > 5$ m s^{-1}, saturation can be assumed. Vertical velocities at or below 5 m s^{-1}, which contain the vast majority of the upward mass flux in TCs (~ 70 %; Black et al. 1996; Braun 2002) are shown to have larger variability in their saturation state and thus, more information is needed.

In the present algorithm, saturation is determined by solving for the net production of precipitation in a reduced form of the precipitation continuity equation. Cloud water production, which occurs when the air is saturated, is shown to explain ~71 % of the variability in the net production of precipitation at all temperatures and ~87 % at temperatures > 0°C. The mechanism for the production of precipitation described by the cloud water is simply the collision-coalescence process (Rogers and Yau 1989). There are errors in the saturation computation due to more complicated physics (mixed-phase regions and cloud boundaries) and when applying the algorithm to Doppler radars (resolution in time/space, attenuation and calibration). A positive aspect of the saturation algorithm is the ability to accept some error as only the *condition* of saturation is necessary for the retrievals.

Latent heating rate sensitivity tests showed that random errors are small (mean of less than 10 %) from the association of saturation with the net production of precipitation. The heating errors are larger from assuming steady-state in the precipitation continuity equation (mean of ~ 20 %). A parameterization for the storage term based largely on the tangential advective flux of precipitation (a consequence of the divergence theorem) was developed that shows promise for reducing the steady-state uncertainties in TCs.

Applying the new algorithm to NOAA P-3 airborne Doppler radar observations, the three- and four-dimensional structure of the latent heat of condensation/evaporation in rapidly intensifying Hurricane Guillermo (1997) is presented. Given the fact that latent heat is the primary energy source for TCs and that considerable uncertainty exists in previous observational studies and numerical model microphysics schemes, the new retrievals could prove quite useful for the community. The dominant source of error in the latent heating magnitude is the vertical velocity with minor contributions from the thermodynamic information. For characteristic errors in vertical velocity from the Guillermo P-3 analyses (Reasor et al. 2009), an uncertainty of ~32 % in the heating magnitude is found for updrafts of 5 m s^{-1} and ~156 % for updrafts of 1 m s^{-1}. Uncertainty in the retrievals due to sampling issues (for updrafts > 5 m s^{-1}) is small (14 %). To augment the P-3 retrievals, the latent heat of condensation from a composite hot tower using nadir-pointing, high-resolution, EDOP data is also computed and shown in Fig. 14 for reference.

Overall, the algorithm does a reasonably good job of retrieving the latent heat field in TCs. Even though errors in the vertical velocity can lead to large uncertainties in the latent heating field for small updrafts/downdrafts, in an integrated sense the errors are not

as drastic. The real test of the usefulness of the latent heat retrievals comes from an analysis of their impacts on the predicted intensity and structure of TCs. To this end, the Guillermo latent heat retrievals are used as forcing in a nonlinear numerical model to examine their impacts on the simulated intensity and structure change of the storm relative to a case that relies on the model's microphysical scheme for forcing. This work is presented in part two.

Acknowledgments. The first author would like to thank Drs. Chris Jeffery and Gerald Heymsfield for providing support for visits to Los Alamos National Laboratory (LANL) and NASA Goddard Space Flight Center (GSFC), respectively as well as excellent feedback on the work. We acknowledge Dr. Robert Black for the particle data and processing in Hurricane Katrina (2005), Dr. Scott Braun for providing numerical model output and discussion, Dr. Robert Hart for extensive feedback and Dr. Matt Eastin for providing a figure or two. This research was supported by the Los Alamos National Laboratory through a project entitled: "Flash Before the Storm: Predicting Hurricane Intensification using LANL Lightning Data" with Dr. Chris Jeffery the PI. In addition, financial support was also provided by a NASA ocean vector winds contract and a NOAA grant to Dr. Mark Bourassa.

REFERENCES

Adler, R.F., and E.B. Rodgers, 1977: Satellite-observed latent heat release in a tropical cyclone. *Mon. Wea. Rev.*, **105,** 956-963.

Black, R.A, 1990: Radar reflectivity-ice water content relationships for use above the melting level in hurricanes. *J. Appl. Meteor.*, **29,** 955-961.

——, G. M. Heymsfield, and J. Hallett, 2003: Extra large particle images at 12 km in a hurricane eyewall: Evidence of high-altitude supercooled water? *Geophys. Res. Lett.* ***30,*** 2124, doi:10.1029/2003GL017864.

Black, M.L., R.W. Burpee, and F.D. Marks, Jr., 1996: Vertical motion characteristics of tropical cyclones determined with airborne Doppler radial velocities. *J. Atmos. Sci.*, **53,** 1887-1909.

Braun, S.A., 2002: A cloud-resolving simulation of Hurricane Bob (1991): Storm structure and eyewall buoyancy. *Mon. Wea. Rev.,* **130**, 1573–1592.

——, M.T. Montgomery, and Z. Pu, 2006: High-resolution simulation of Hurricane Bonnie (1998). Part I: The organization of eyewall vertical motion. *J. Atmos. Sci.*, **63,** 19-42.

——, 2006: High-resolution simulation of Hurricane Bonnie (1998). Part II: Water budget. *J. Atmos. Sci.*, **63,** 43-64.

Cecil, D. J., and E. J. Zipser, 1999: Relationships between tropical cyclone intensity and satellite-based indicators of inner core convection: 85-GHz ice-scattering signature and lightning. *Mon. Wea. Rev.,* **127,** 103-123.

Charney, J.G., and A. Eliassen, 1964: On the growth of the hurricane depression. *J. Atmos. Sci.*, **21,** 68-75.

Doviak, R.J., and D.S. Zrnic, 1984: *Doppler Radar and Weather Observations*. Academic Press, 458 pp.

Eastin, M.D., W.M. Gray, and P.G. Black, 2005: Buoyancy of convective vertical motions in the inner core of intense hurricanes. Part I: General statistics. *Mon. Wea. Rev.*, **133,** 188-208.

Emanuel, K.A., 1986: An air-sea interaction theory for tropical cyclones. Part I: Steady-state maintenance. *J. Atmos. Sci.*, **43,** 2044-2061.

Gamache, J.F., R.A. Houze, Jr., and F.D. Marks, Jr., 1993: Dual-aircraft investigation of the inner core of Hurricane Norbert. Part III: Water budget. *J. Atmos. Sci.*, **50,** 3221-

3243.

——, F. D. Marks, Jr., and F. Roux, 1995: Comparison of three airborne Doppler sampling techniques with airborne in situ wind observations in Hurricane Gustav (1990). *J. Atmos. and Oceanic Technol.,* **12,** 171–181.

——, 1997: Evaluation of a fully three-dimensional variational Doppler analysis technique. Preprints, *28th Conf. on Radar Meteorology*, Austin, TX, Amer. Meteor. Soc., 422-423.

Gao, J., M. Xue, A. Shaprio, and K.K. Droegemeier, 1999: A variational method for the analysis of three-dimensional wind fields from two Doppler radars. *Mon. Wea. Rev.*, **127,** 2128-2142.

Guimond, S.R., G.M. Heymsfield, and F.J. Turk, 2010: Multiscale observations of Hurricane Dennis (2005): The effects of hot towers on rapid intensification. *J. Atmos. Sci.*, **67,** 633-654.

Hack J. J., and W. H. Schubert, 1986: Nonlinear response of atmospheric vortices to heating by organized cumulus convection. *J. Atmos. Sci.*, **43,** 1559–1573.

Heymsfield, G.M., and Coauthors, 1996: The EDOP radar system on the high-altitude NASA ER-2 aircraft. *J. Atmos. Oceanic Technol.,* **13,** 795-809.

——, J.B. Halverson, and I.J. Caylor, 1999: A wintertime Gulf Coast squall line observed by EDOP airborne Doppler radar. *Mon. Wea. Rev.,* **127,** 2928-2949.

——, J.B. Halverson, J. Simpson, L. Tian, and T.P. Bui, 2001: ER-2 Doppler radar investigations of the eyewall of Hurricane Bonnie during the Convection and Moisture Experiment-3. *J. Appl. Meteor.,* **40,** 1310-1330.

——, L. Tian, A.J. Heymsfield, L. Li, and S. Guimond, 2010: Characteristics of deep tropical and subtropical convection from nadir-viewing high-altitude airborne Doppler radar. *J. Atmos. Sci.*, **67,** 285-308.

Houze, R.A., Jr., 1993: *Cloud Dynamics*. Academic Press, 573 pp.

Kuo, H.L., 1965: On formation and intensification of tropical cyclones through latent heat release by cumulus convection. *J. Atmos. Sci.*, **22,** 40-63.

Marks, F.D., Jr., R.A. Houze, Jr., and J.F. Gamache, 1992: Dual-aircraft investigation of the inner core of Hurricane Norbert. Part I: Kinematic structure. *J. Atmos. Sci.*, **49,** 919-942.

McFarquhar, G.M., H. Zhang, G. Heymsfield, R. Hood, J. Dudhia, J.B. Halverson, and F. Marks, Jr., 2006: Factors affecting the evolution of Hurricane Erin (2001) and the

distributions of hydrometeors: Role of microphysical processes. *J. Atmos. Sci.*, **63,** 127-150.

Morrow, C.R., 2008: An expanding database of dual-Doppler tropical cyclone observations. M.S. thesis, Dept. of Meteorology, The Florida State University, 146 pp.

Nolan, D.S., and L.D. Grasso, 2003: Three-dimensional, nonhydrostatic perturbations to balanced, hurricane-like vortices. Part II: Symmetric response and nonlinear simulations. *J. Atmos. Sci.*, **60,** 2717-2745.

——, Y. Moon, and D.P.Stern, 2007: Tropical cyclone intensification from asymmetric convection: Energetics and efficiency. *J. Atmos. Sci.*, **64,** 3377-3405.

Petty, G.W., 2006: *A First Course in Atmospheric Radiation*. Sundog Publishing, 459 pp.

Reasor, P.D., M.T. Montgomery, F.D. Marks, Jr., and J.F. Gamache, 2000: Low-wavenumber structure and evolution of the hurricane inner core observed by airborne dual-Doppler radar. *Mon. Wea. Rev.*, **128,** 1653-1680.

——, M.D. Eastin, and J.F. Gamache, 2009: Rapidly intensifying Hurricane Guillermo (1997). Part I: Low-wavenumber structure and evolution. *Mon. Wea. Rev.*, **137,** 603-631.

Rodgers, E., W. Olson, J. Halverson, J. Simpson, and H. Pierce, 2000: Environmental forcing of Supertyphoon Paka's (1997) latent heat structure. *J. Appl. Meteor.*, **39,** 1983-2006.

Rogers, R.R., and M.K. Yau, 1989: *A Short Course in Cloud Physics.* Butterworth-Heinemann publishers, 304 pp.

Rogers, R.F., M.L. Black, S.S. Chen, and R.A. Black, 2007: An evaluation of microphysics fields from mesoscale model simulations of tropical cyclones. Part I: Comparisons with observations. *J. Atmos. Sci.*, **64,** 1811-1834.

Roux, F., 1985: Retrieval of thermodynamic fields from multiple-Doppler radar data using the equations of motion and the thermodynamic equation. *Mon. Wea. Rev.*, **113,** 2142-2157.

——, and S. Ju, 1990: Single-Doppler observations of a west African squall line on 27-28 May 1981 during COPT 81: Kinematics, thermodynamics and water budget. *Mon. Wea. Rev.*, **118,** 1826-1854.

Sitkowski M., and G. M. Barnes, 2009: Low-level thermodynamic, kinematic, and reflectivity fields of Hurricane Guillermo (1997) during rapid intensification. *Mon.*

Wea. Rev., **137,** 645–663.

Tao, W.-K. and Coauthors, 2006: Retrieval of latent heating from TRMM measurements. *Bull. Amer. Meteor. Soc.*, **87,** 1555-1572.

Tong, H., V. Chandrasekar, K.R. Knupp, and J. Stalker, 1998: Multiparameter radar observations of time evolution of convective storms: Evaluation of water budgets and latent heating rates. *J. Atmos. Oceanic Technol.*, **15,** 1097-1109.

Tory, K. J., M. T. Montgomery, and N. E. Davidson, 2006: Prediction and diagnosis of tropical cyclone formation in an NWP system. Part I: The critical role of vortex enhancement in deep convection. *J. Atmos. Sci.,* **63,** 3077-3090.

Ulbrich, C. W., and P. B. Chilson, 1994: Effects of variations in precipitation size distribution and fallspeed law parameters on relations between mean Doppler fallspeed and reflectivity factor. *J. Atmos. Oceanic Technol.,* **11,** 1656–1663.

Wimmers, A.J., and C.S. Velden, 2007: MIMIC: A new approach to visualizing satellite microwave imagery of tropical cyclones. *Bull. Amer. Meteor. Soc.*, **88,** 1187-1196.

Zhang, D.-L., Y. Liu, and M.K. Yau, 2002: A multiscale numerical study of Hurricane Andrew (1992). Part V: Inner-core thermodynamics. *Mon. Wea. Rev.*, **130,** 2745-2763.

FIGURE CAPTIONS

1. The top five maximum updraft profiles in the TC eyewall from the Heymsfield et al. (2010) population. The gray lines show each member with the black line representing the mean. See Heymsfield et al. (2010) for more information.

2. NOAA P-3 lower fuselage radar (5.3 GHz) reflectivity at 3-km height during the center of each aircraft pass through Hurricane Guillermo (1997). The domain is 120 km on each side with tick marks every 15 km. The solid arrow in pass 1 represents the time-averaged, local shear vector and the capital letters denote details of the convective bursts. Figure is taken from Reasor et al. (2009). Used with permission of the AMS.

3. Aircraft (P-3) flight level (between 1.5 to 5.5 km altitude) measurements of updraft core magnitude as a function of relative humidity from the eyewall and rainband regions of intense TCs. Note that there are 620 data points in the figure. The figure is courtesy of Matt Eastin; see Eastin et al. (2005) for details.

4. Relationship between the source of cloud water and the net production of precipitation for grid points where precipitation is produced in the model domain between 0 and 10 km height and over a nine minute period (with three minute output). Data is from the numerical simulation of Hurricane Bonnie (1998; Braun 2006). The black line shows the linear fit to the data with an R^2 of ~0.70 found using all 60 minutes of model output. The red and blue circles denote warm ($T > 0°C$) and mixed/ice ($T \leq 0°C$) phase precipitation

processes, respectively. An R^2 of ~0.87 is found applying the linear fit to the red points only over a 60 minute period. The contour lines show the number of points in dense regions of the scatter plot. Black contours start at 500 with a 500 point interval while white contours start at 3000 with a 6000 point interval. There are a total of 828,611 points in the figure with the largest percentage located in the lower left corner (> 15,000 points.

5. A typical profile of the net source of precipitation (black line) and the source of cloud water (green line) through deep eyewall convection from the numerical simulation of Hurricane Bonnie (1998; Braun 2006). The profiles are averaged over a 10 km by 10 km horizontal region centered on a convective cell for one snapshot in time. The blue line indicates the freezing level.

6. Flowchart summarizing the basic steps in the LH retrieval algorithm. These steps are performed at each grid point in the Doppler analysis domain. All variables and equations, including approximations are defined in the text.

7. The relationship between the horizontal advective flux of precipitation (in brackets on right-hand-side of equation 5) and the storage of precipitation for model grid points where precipitation is produced at one snapshot in time. Model data is from Hurricane Bonnie (1998; Braun 2006) using 2 km horizontal resolution. The fit (see text) explains 78% of the variance in the data.

8. The impact of the model-derived storage term parameterization on computations of Q_{net} (using equation 2) in terms of the RMSE (averaged over the model domain). The control is Q_{net} output directly from the model. The black line shows the results for computing Q_{net} using the steady state assumption and the red line using the parameterization (equation 5). In addition, the green line shows the impact of using the complete reduced form of the precipitation continuity equation (2) to calculate Q_{net}. The blue dashed line shows the mean value of Q_{net} for reference.

9. Same as Fig. 8 only the chosen measure of error is the azimuthal mean integration for Q_{net}. The mean values over time for each case are: steady state (~27%), parameterization (~11%) and reduced form (~1%).

10. The impact of the model-derived storage term parameterization on the azimuthal mean heating at the RMW for the Guillermo Doppler analyses. The thick black line shows the time mean and the shading depicts the standard error of the mean.

11. The error (according to equation 6) in computing latent heat by determining saturation using the algorithm described in the text (use equations (2) and (5) to determine where the values of Q_{net} are greater than zero). The control is computing latent heat where model grid points are producing cloud water. The heating rates are computed according to equation (4) with the figure showing results for updrafts only. The temporal mean error is ~8%.

12. The relationship between radar reflectivity factor (expressed in dBZ) and liquid water content using cloud particle data (~ 7,000 data points) from NOAA P-3 aircraft flying at ~ 4 km altitude in Hurricane Katrina (2005) during a mature stage of the storm. The red line shows the best-fit nonlinear model ($Z = 402 \times LWC^{1.47}$) and the blue lines represent the 95% confidence interval. The correlation coefficient is 0.88.

13. Three-dimensional isosurfaces of the latent heat of condensation (red, 100 K h^{-1}) and evaporation (blue, -100 K h^{-1}) retrieved from airborne Doppler radar observations in Hurricane Guillermo (1997) at the times shown in Fig. 2. The grid volume is storm-centered extending 120 km on each side and 19 km in the vertical with a grid spacing of 2 km in the horizontal and 1 km in the vertical. The first useful level is at 1 km due to ocean surface contamination.

14. Profile of the LH of condensation (K h^{-1}) for the mean EDOP hot tower profile shown in Fig. 1. See text for details.

15. Comparison of P-3 flight level (~3 km altitude) and Doppler radar retrieved vertical velocity for a radial penetration into Hurricane Guillermo valid at ~2002 UTC 2 August 1997. Figure is from Morrow (2008). See Reasor et al. (2009) for details of the comparisons.

16. Histogram of Doppler radar retrieved latent heating rates for vertical velocities > 5 m s^{-1} in Hurricane Guillermo on 2 August 1997.

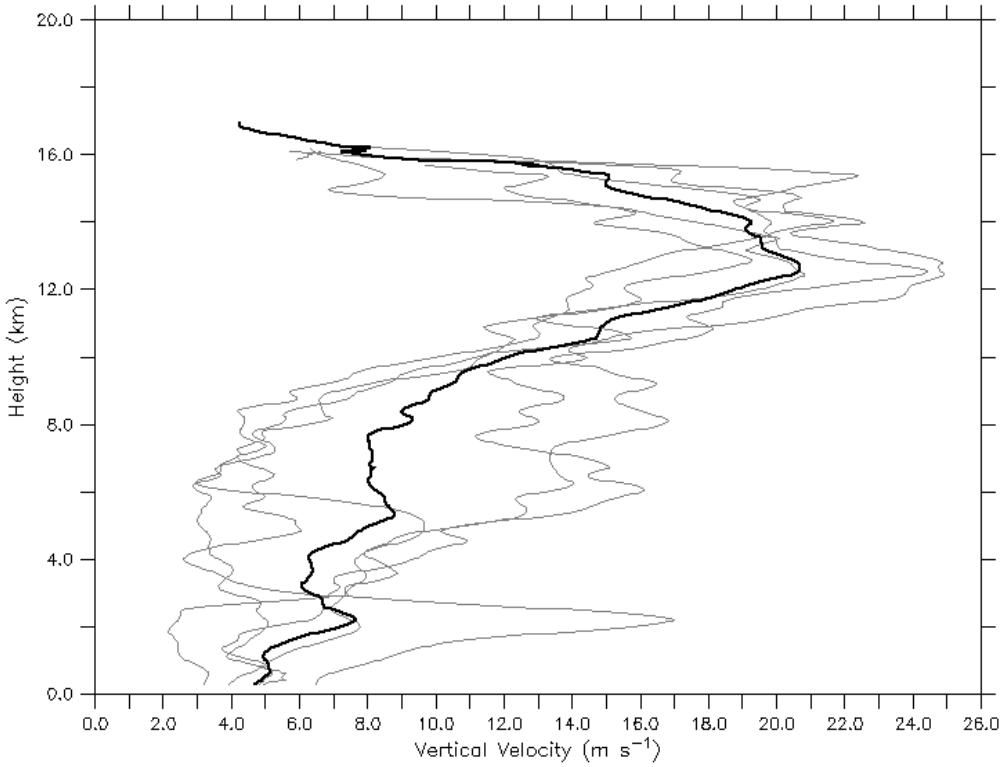

Figure 1. The top five maximum updraft profiles in the TC eyewall from the Heymsfield et al. (2010) population. The gray lines show each member with the black line representing the mean. See Heymsfield et al. (2010) for more information.

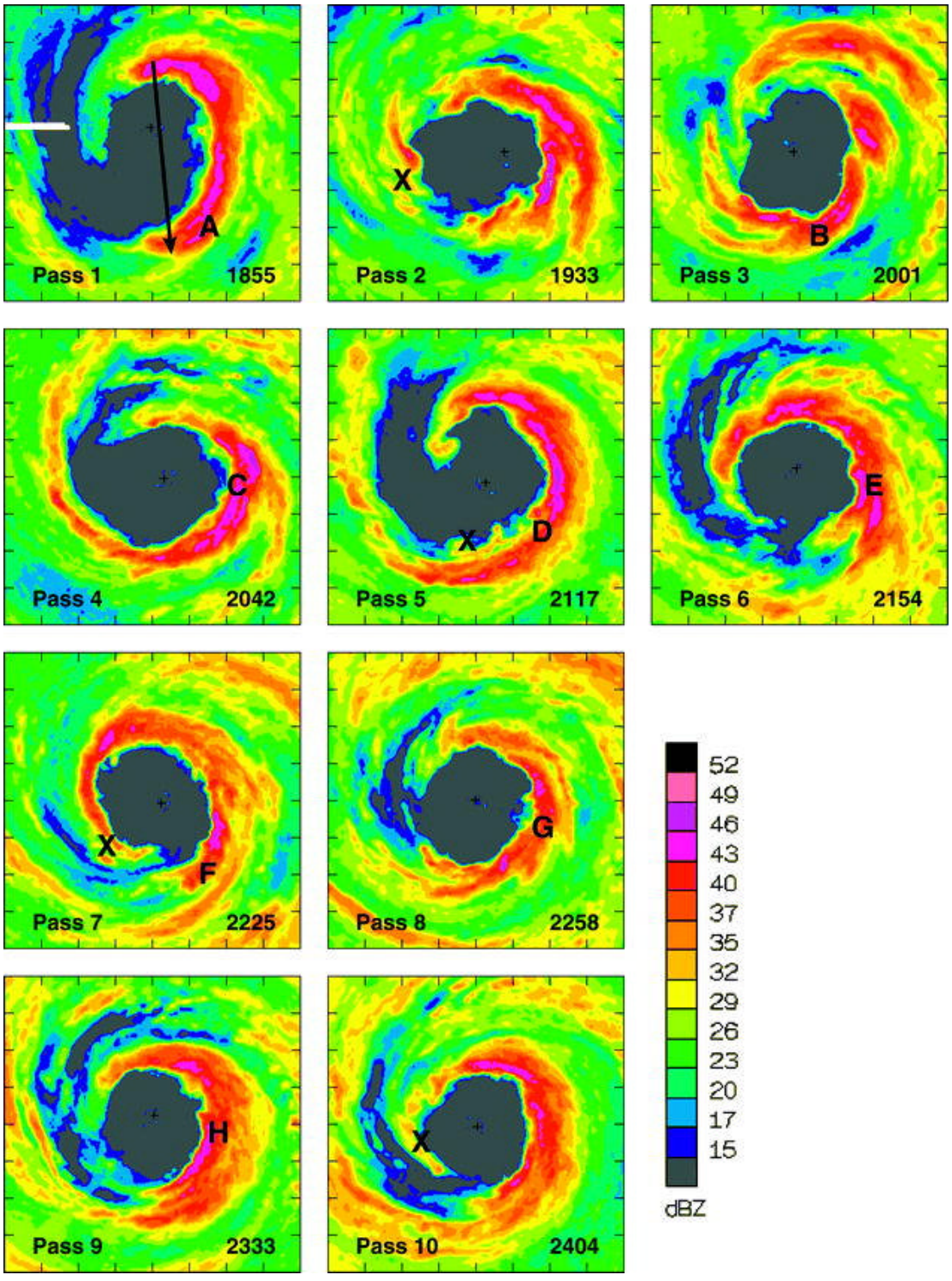

Figure 2. NOAA P-3 lower fuselage radar (5.3 GHz) reflectivity at 3-km height during the center of each aircraft pass through Hurricane Guillermo (1997). The domain is 120 km on each side with tick marks every 15 km. The solid arrow in pass 1 represents the time-averaged, local shear vector and the capital letters denote details of the convective bursts. Figure is taken from Reasor et al. (2009). Used with permission of the AMS.

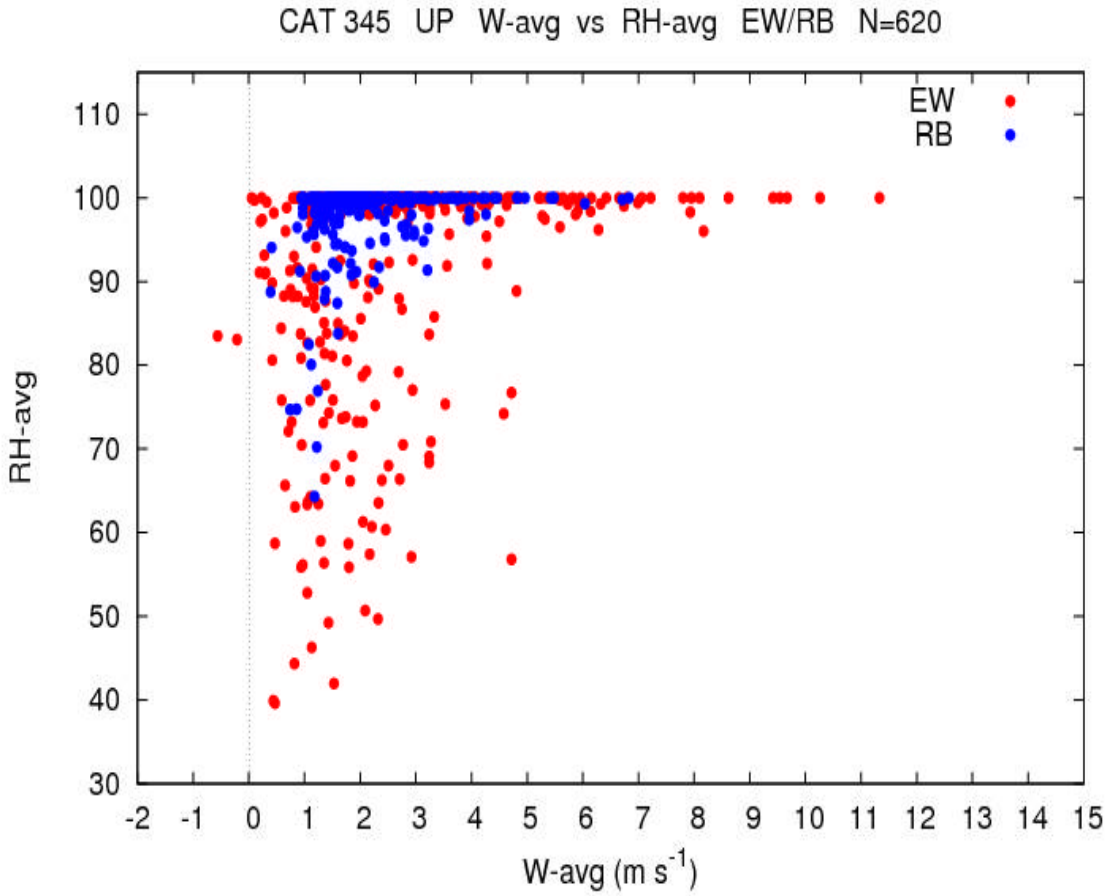

Figure 3. Aircraft (P-3) flight level (between 1.5 to 5.5 km altitude) measurements of updraft core magnitude as a function of relative humidity from the eyewall and rainband regions of intense TCs. Note that there are 620 data points in the figure. The figure is courtesy of Matt Eastin; see Eastin et al. (2005) for details.

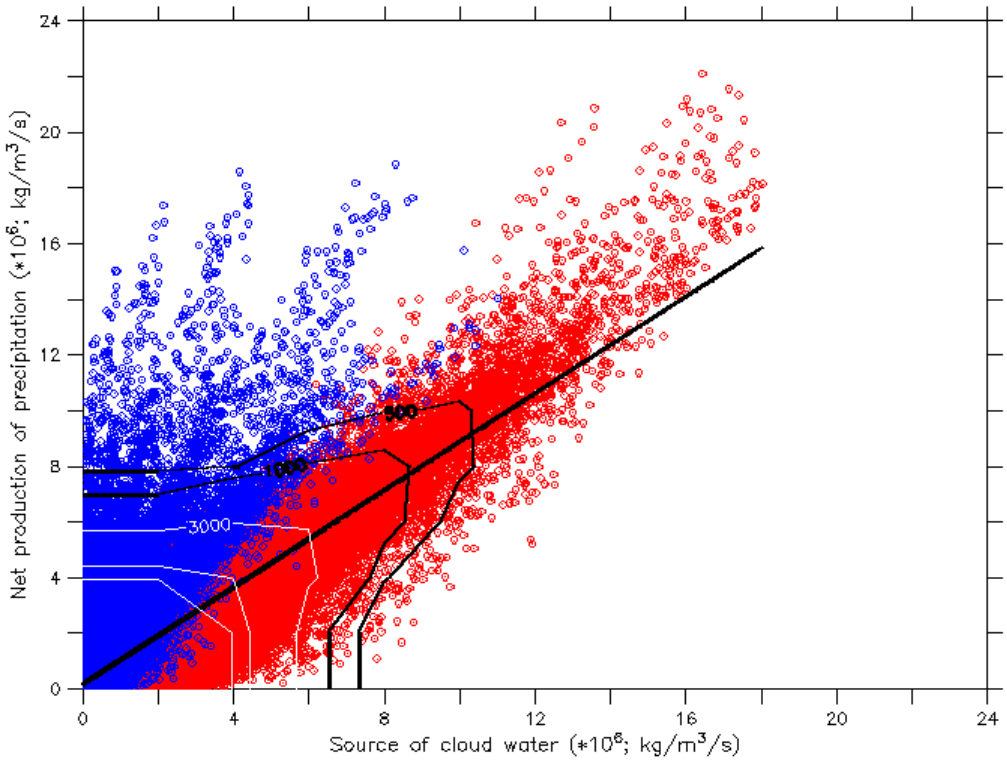

Figure 4. Relationship between the source of cloud water and the net production of precipitation for grid points where precipitation is produced in the model domain between 0 and 10 km height and over a nine minute period (with three minute output). Data is from the numerical simulation of Hurricane Bonnie (1998; Braun 2006). The black line shows the linear fit to the data with an R^2 of ~0.70 found using all 60 minutes of model output. The red and blue circles denote warm ($T > 0°C$) and mixed/ice ($T \leq 0°C$) phase precipitation processes, respectively. An R^2 of ~0.87 is found applying the linear fit to the red points only over a 60 minute period. The contour lines show the number of points in dense regions of the scatter plot. Black contours start at 500 with a 500 point interval while white contours start at 3000 with a 6000 point interval. There are a total of 828,611 points in the figure with the largest percentage located in the lower left corner (> 15,000 points).

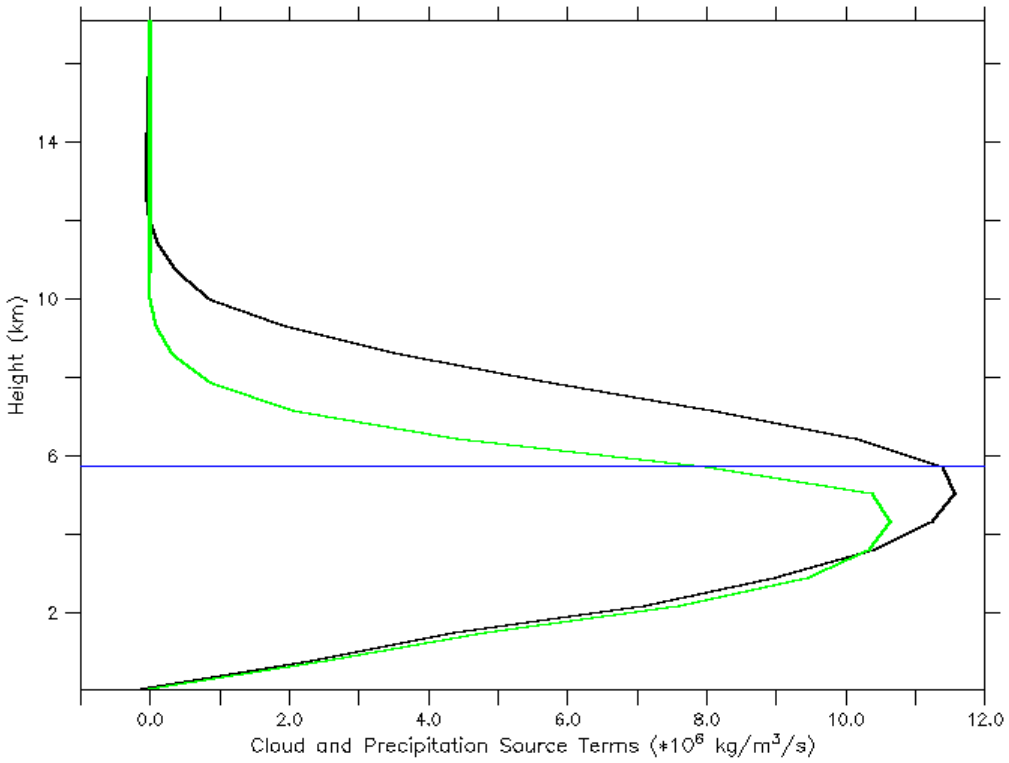

Figure 5. A typical profile of the net source of precipitation (black line) and the source of cloud water (green line) through deep eyewall convection from the numerical simulation of Hurricane Bonnie (1998; Braun 2006). The profiles are averaged over a 10 km by 10 km horizontal region centered on a convective cell for one snapshot in time. The blue line indicates the freezing level.

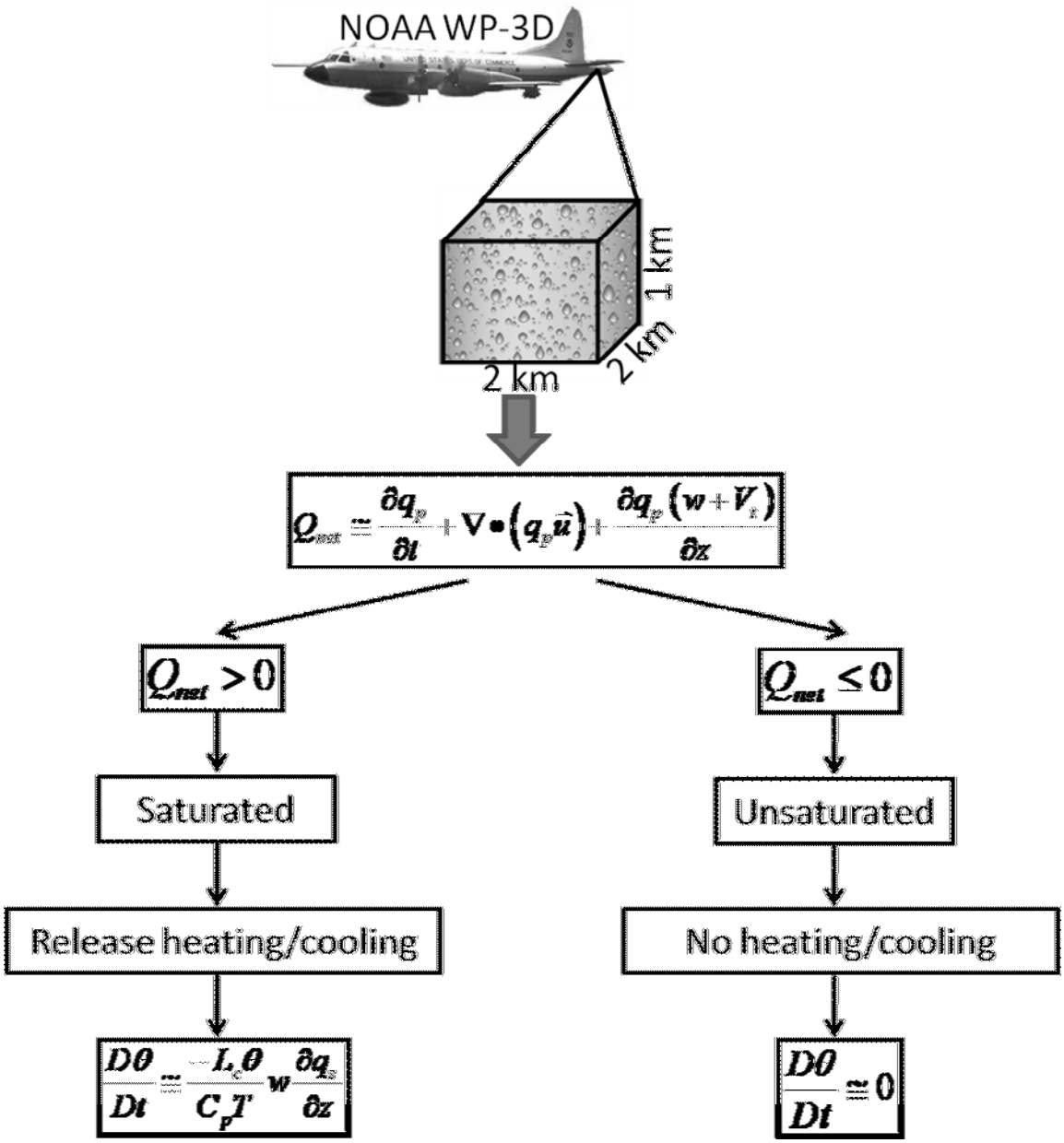

Figure 6. Flowchart summarizing the basic steps in the LH retrieval algorithm. These steps are performed at each grid point in the Doppler analysis domain. All variables and equations, including approximations are defined in the text.

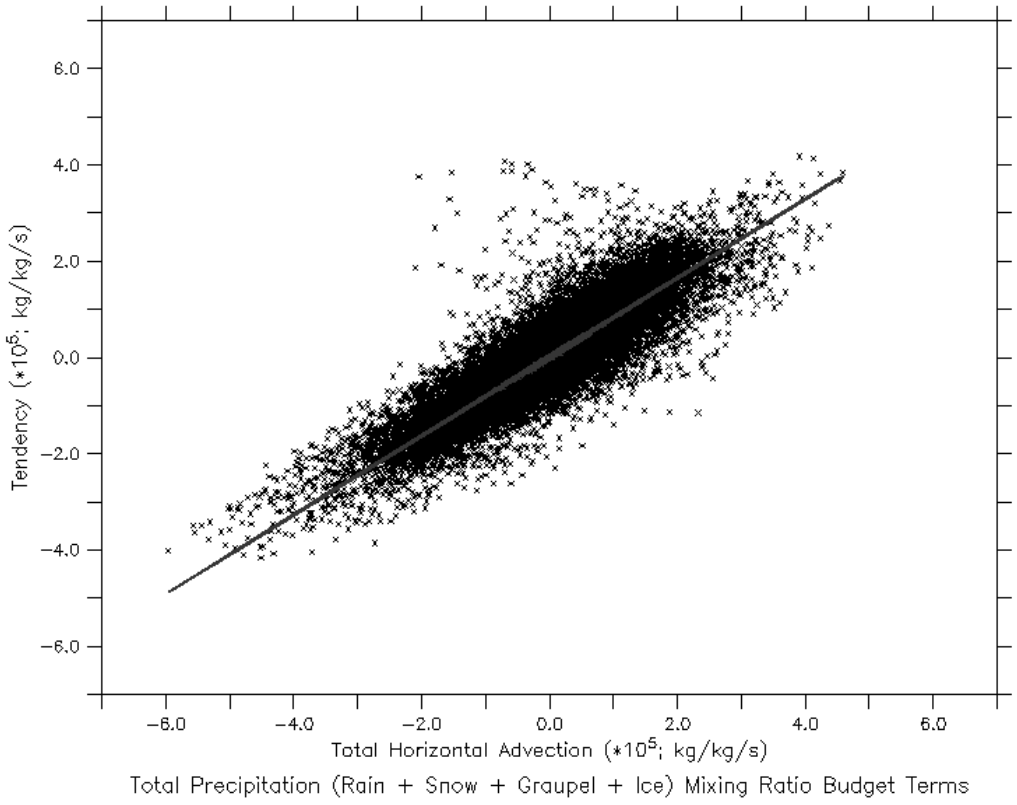

Figure 7. The relationship between the horizontal advective flux of precipitation (in brackets on right-hand-side of equation 5) and the storage of precipitation for model grid points where precipitation is produced at one snapshot in time. Model data is from Hurricane Bonnie (1998; Braun 2006) using 2 km horizontal resolution. The fit (see text) explains 78% of the variance in the data.

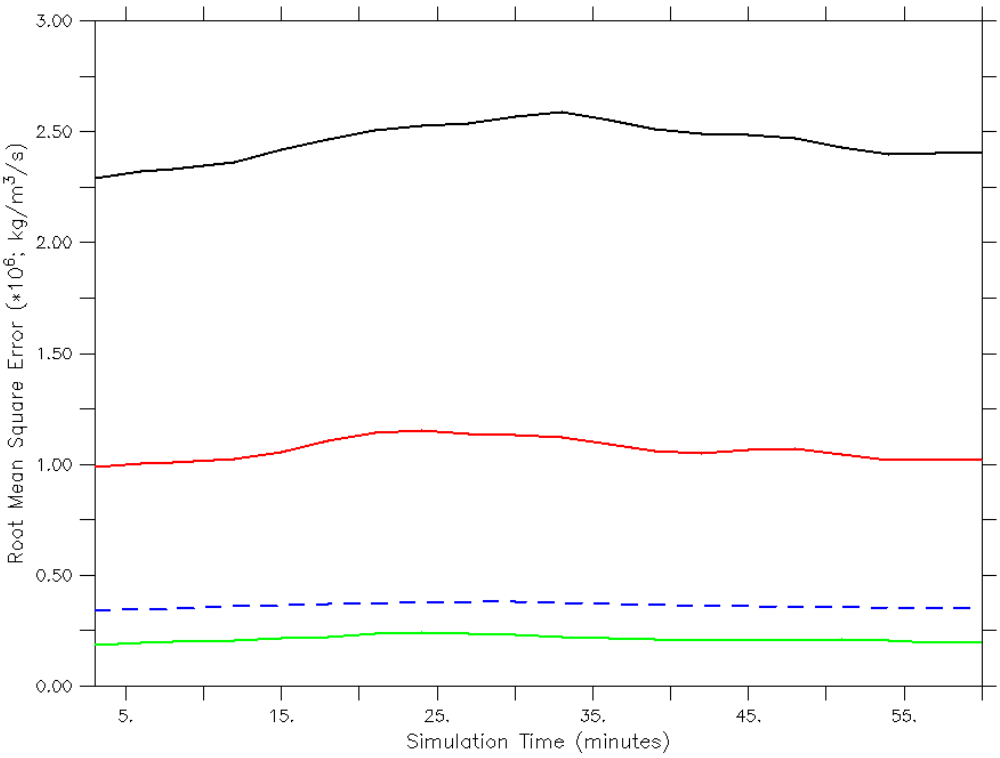

Figure 8. The impact of the model-derived storage term parameterization on computations of Q_{net} (using equation 2) in terms of the RMSE (averaged over the model domain). The control is Q_{net} output directly from the model. The black line shows the results for computing Q_{net} using the steady state assumption and the red line using the parameterization (equation 5). In addition, the green line shows the impact of using the complete reduced form of the precipitation continuity equation (2) to calculate Q_{net}. The blue dashed line shows the mean value of Q_{net} for reference.

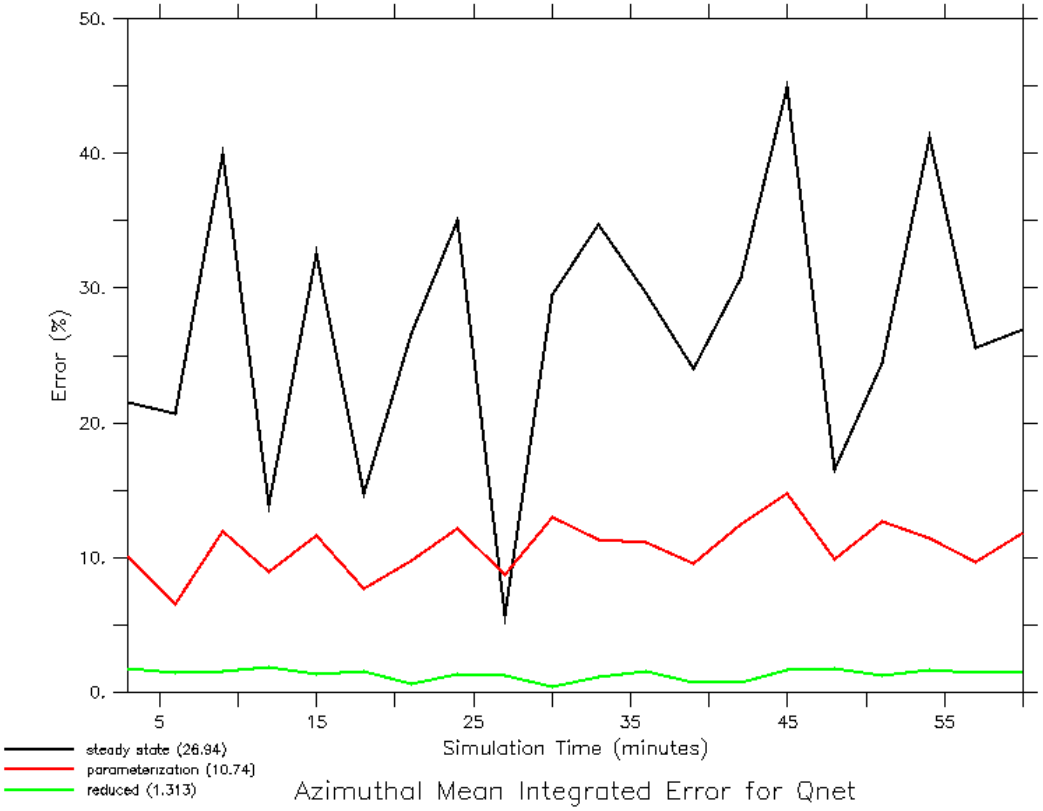

Figure 9. Same as Fig. 8 only the chosen measure of error is the azimuthal mean integration for Q_{net}. The mean values over time for each case are: steady state (~27%), parameterization (~11%) and reduced form (~1%).

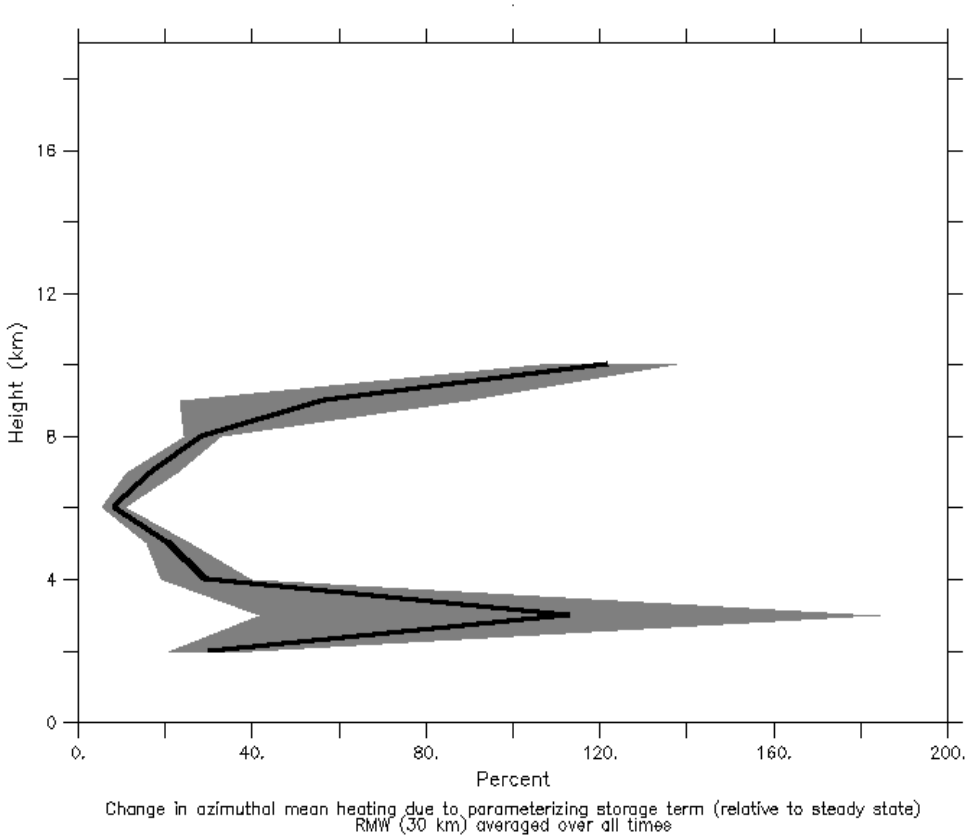

Figure 10. The impact of the model-derived storage term parameterization on the azimuthal mean heating at the RMW for the Guillermo Doppler analyses. The thick black line shows the time mean and the shading depicts the standard error of the mean.

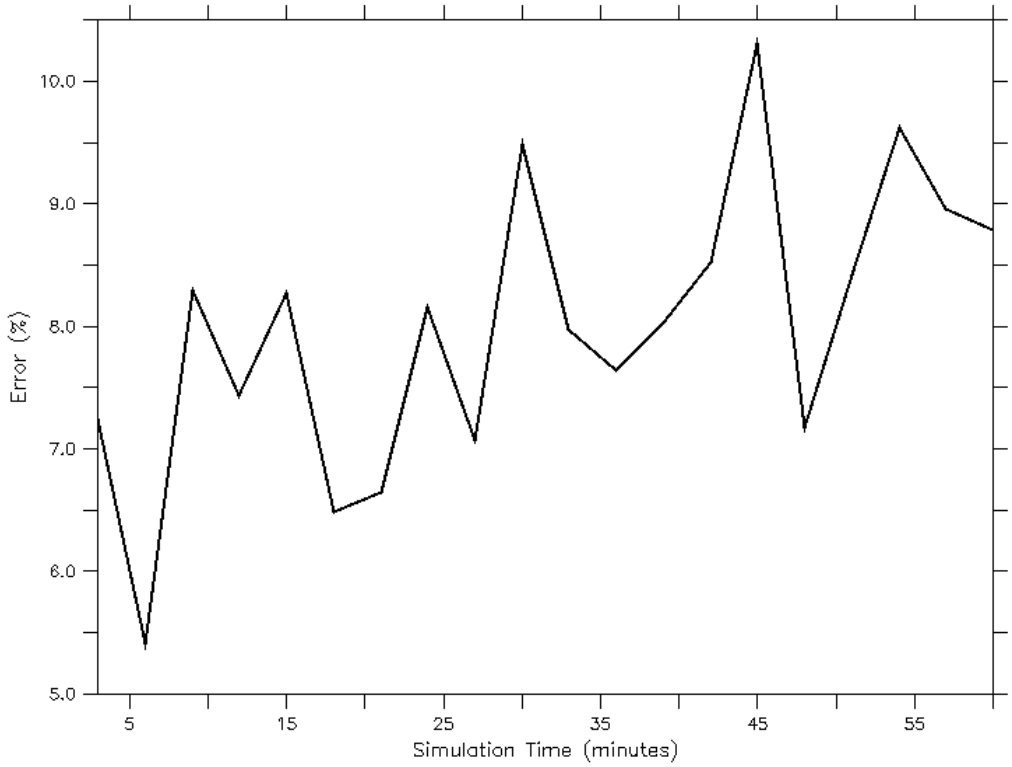

Figure 11. The error (according to equation 6) in computing latent heat by determining saturation using the algorithm described in the text (use equations (2) and (5) to determine where the values of Q_{net} are greater than zero). The control is computing latent heat where model grid points are producing cloud water. The heating rates are computed according to equation (4) with the figure showing results for updrafts only. The temporal mean error is ~8%.

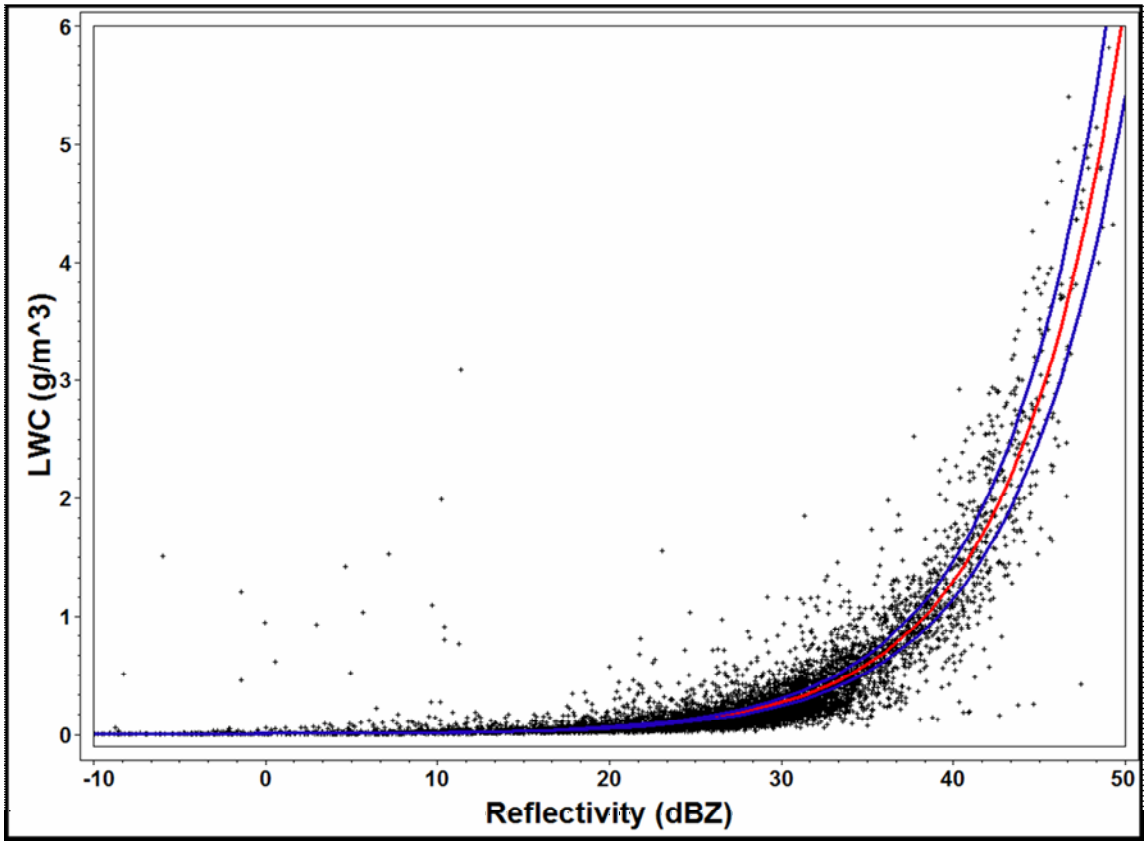

Figure 12. The relationship between radar reflectivity factor (expressed in dBZ) and liquid water content using cloud particle data (~ 7,000 data points) from NOAA P-3 aircraft flying at ~ 4 km altitude in Hurricane Katrina (2005) during a mature stage of the storm. The red line shows the best-fit nonlinear model ($Z = 402 \times LWC^{1.47}$) and the blue lines represent the 95% confidence interval. The correlation coefficient is 0.88.

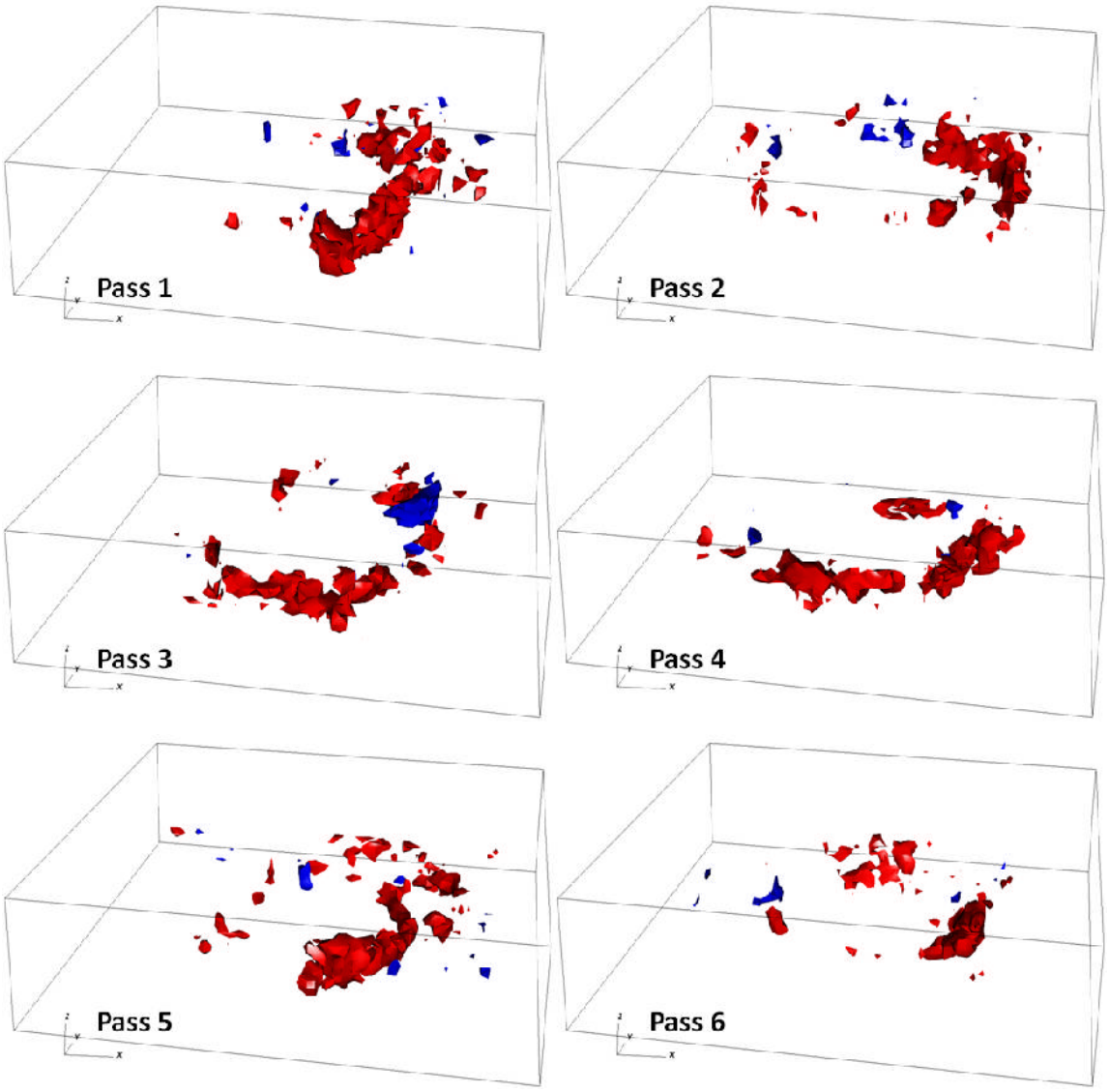

Figure 13. Three-dimensional isosurfaces of the latent heat of condensation (red, 100 K h^{-1}) and evaporation (blue, -100 K h^{-1}) retrieved from airborne Doppler radar observations in Hurricane Guillermo (1997) at the times shown in Fig. 2. The grid volume is storm-centered extending 120 km on each side and 19 km in the vertical with a grid spacing of 2 km in the horizontal and 1 km in the vertical. The first useful level is at 1 km due to ocean surface contamination.

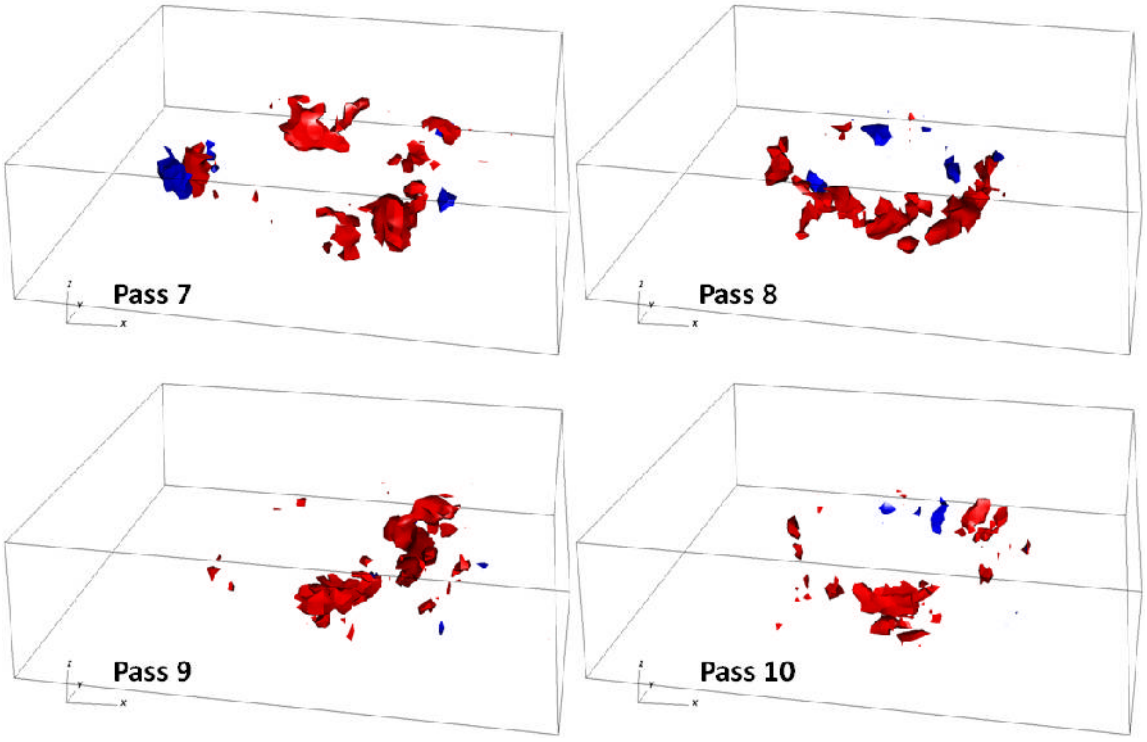

Figure 13. continued.

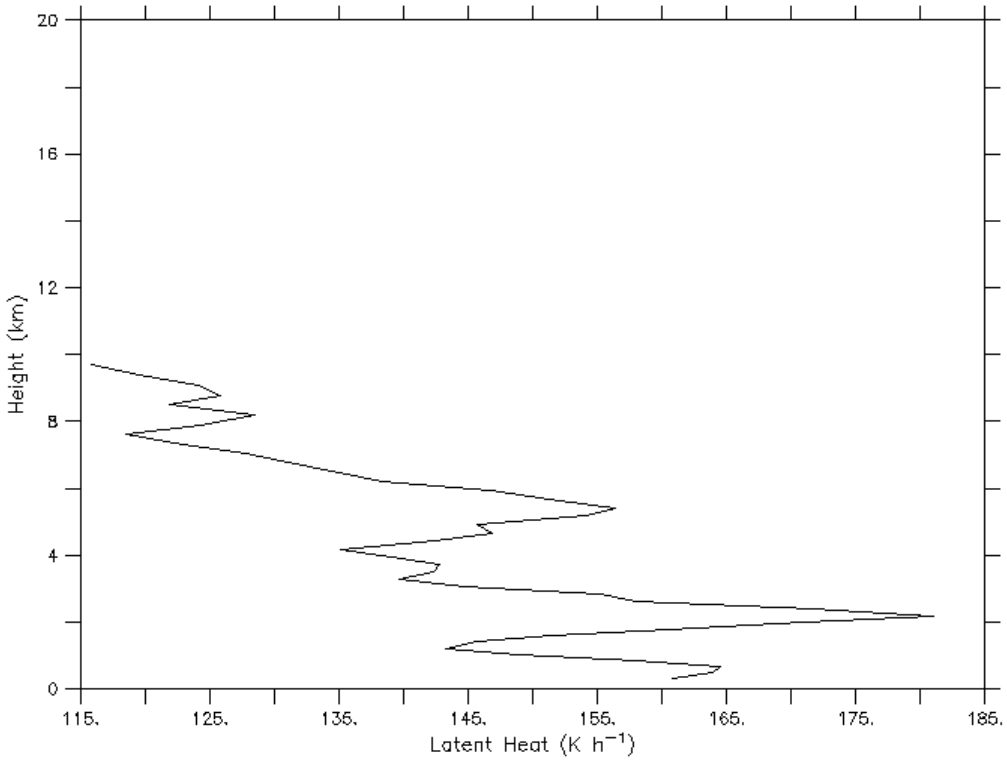

Figure 14. Profile of the LH of condensation (K h^{-1}) for the mean EDOP hot tower profile shown in Fig. 1. See text for details.

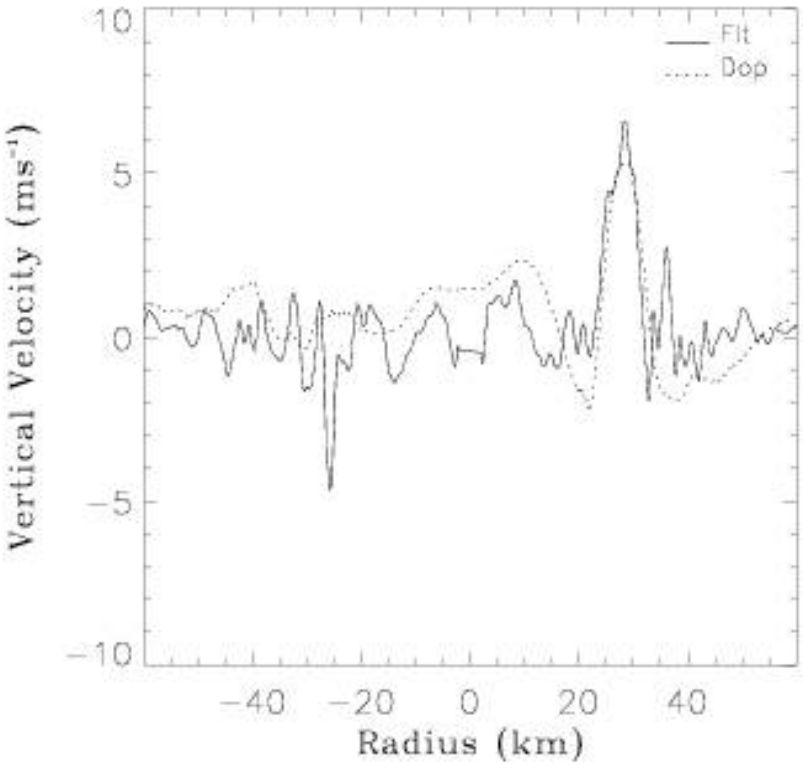

Figure 15. Comparison of P-3 flight level (~3 km altitude) and Doppler radar retrieved vertical velocity for a radial penetration into Hurricane Guillermo valid at ~2002 UTC 2 August 1997. Figure is from Morrow (2008). See Reasor et al. (2009) for details of the comparisons.

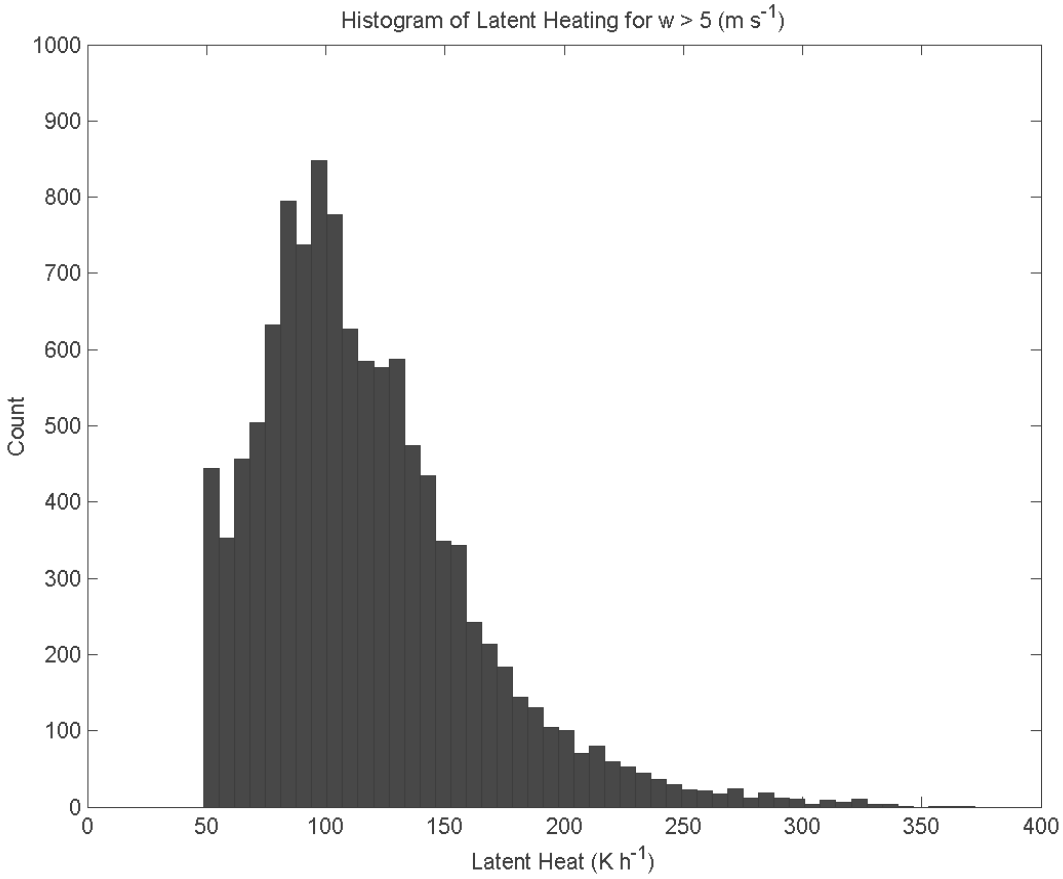

Figure 16. Histogram of Doppler radar retrieved latent heating rates for vertical velocities > 5 m s^{-1} in Hurricane Guillermo on 2 August 1997.